




Hydrogeochemical Conditions in Groundwater Systems with Various Geomorphological Units in Kulonprogo Regency, Java Island, Indonesia

Reinaldy Pratama Poetra¹ · Tjahyo Nugroho Adji¹  · Langgeng Wahyu Santosa¹ · Nurul Khakhim²

Received: 9 April 2020 / Accepted: 15 June 2020 / Published online: 24 June 2020
© Springer Nature B.V. 2020

Abstract

Geomorphological (landform) aspects have long been known to control groundwater conditions in an area. Thus, combining the hydrogeological and geomorphological aspects (lithology, genesis, and morphology) becomes a prospective approach for understanding and delineating the hydrogeochemical processes in an area. The idea is then applied in Kulonprogo, Java, Indonesia, that consists of several landforms with minimum anthropogenic influence, in order to identify and quantify the hydrogeochemical processes that are responsible for hydrogeochemical facies changes in each landform. The groundwater facies based on Kurlov classification in each landform are strongly influenced by the water–rock interaction process as it presented in the Gibbs curve. The magnitude of saturation indices and mass transfer is also diverse that caused a distinction of hydrogeochemical facies and processes in each landform. For instance, the evolution of groundwater in the denudational hill to the fluvio-marine plain occurs from Ca-HCO_3 to Na+K-Ca-HCO_3 . The analysis of Durov diagram and inverse modeling—using PHREEQ—reveals that the hydrogeochemical processes that occur in most of the landform are ion exchange, weathering or dissolution, and precipitation. Further, oxidation–reduction and mixing only occur in few landforms. The further investigation from mass balance calculation that constructs from inverse modeling reveals some interesting findings and hypotheses, such as the construction of gypsum probably found in the deeper layer on swale as a result of pyrite dissolution of 1.074×10^{-3} mmol, and it is responsible in escalating Ca^{2+} and SO_4^{2-} . Another finding is that although the calcite mineral mostly related to the past-marine environment, such as in the east denudational hill, the calcite in the west part is formed as a breakdown of 3.225×10^{-3} mmol anorthite.

Keywords Hydrogeochemistry · Landforms · Minerals · Saturation indices · Mass balance modeling

✉ Tjahyo Nugroho Adji
adji_tjahyo@ugm.ac.id

¹ Department of Environmental Geography, Faculty of Geography, Universitas Gadjah Mada, Sekip Utara, Bulaksumur, Yogyakarta 55281, Indonesia

² Department of Geographic Information Science, Faculty of Geography, Universitas Gadjah Mada, Yogyakarta 55281, Indonesia

1 Introduction

Geological and geomorphological configurations have a strong influence on groundwater conditions (Adji and Sejati 2014). Geological configuration and rock stratigraphy control the direction of groundwater flow, type, depth, and thickness of aquifers. Lithological conditions also affect aquifer permeability and dissolved ion concentrations in the groundwater. In terms of geophysics, morphology (the relief of the Earth's surface) and morphogenesis (the formation of landforms or other structures), both greatly influence groundwater conditions. Morphology also controls the direction of groundwater flow because the variability of topography affects the groundwater level in an area.

Geomorphology is the study of landforms, their origin, evolution, and distribution at the surface of the Earth. Landforms have four aspects, two of which are morphology and morphogenesis. Morphology—associated with topographic conditions and reliefs—has control over the groundwater flow path and the residence time. Morphogenesis (passive)—that depends on lithology plus Earth's crust movement (tectonics)—influences hydrogeochemical characteristics because there is a water–rock interaction between typical minerals in a landform and the groundwater. The existence of a typical mineral in each landform also indicates the typical hydrogeochemical processes. Each landform unit has different morphological and morphogenetic attributes, so that its boundary can be delineated from the typical characteristics of each constituent aspect. Verstappen (1983) explained that morphogenesis is an aspect related to the origin and the development or evolution of landforms.

Further, it is possible if there are similar or even identical landforms with different lithology, even in relatively narrow areas. This is caused by the typical process and parent materials in an area. In detailed observation for mapping purposes, this distinguished needs to be done by using lithology as a final delineator. For instance, in the case of the studied area, there are two major parent materials, i.e., volcanic rocks from Old-andesite formation and carbonate rocks from Sentolo formation. This configuration generates identical landform but with a different attribute, especially in terms of the lithology, where there are clayey alluvial plain and alluvial plain of carbonate gravels. Therefore, this explanation indicates that each (detailed) landform should have typical characteristics such as lithology. This idea reinforced by Huggett (2011), who stated that one of the geomorphological components is the constitution (the material properties) from both a physical and chemical perspective. Concerning hydrogeological conditions, this means that morphogenesis affects the permeability, porosity, infiltration rate, and chemical properties of groundwater because each landform will have different lithology and materials. Summerfield (2013) also explained that within a landform unit, there would be typical attributes (such as materials) resulting from the processes at work there. Therefore, the presence of minerals in rocks is closely related to both the regional geological formation and the geomorphology. Minerals are one of the typical attributes of a landform (Huggett 2011; Zinck et al. 2016). Consequently, the spatial distribution of landforms can indicate a variety of mineral types in aquifers within an area. This information suggests that groundwater chemistry varies spatially as a consequence of the diversity of water–rock interaction processes.

The chemical composition mostly determines groundwater quality. The identification of hydrogeochemical properties is generally carried out by analyzing the dissolved ions, hardness, acidity (pH), fluid conductivity (EC), and alkalinity. Groundwater hydrochemistry is the key to understanding the origin, geochemical processes, hydrodynamics, and groundwater interactions with aquifers (Furi et al. 2012). Schot and van der Wal (1992) and Dragon and Gorski (2012) both explained that groundwater hydrochemistry is influenced

by two factors: natural and anthropogenic factors. Within the list of natural factors, Khatri and Tyagi (2015) included the characteristics of aquifers (geology), rocks (types and processes), climate, vegetation, and even natural disasters (droughts, floods, earthquakes, and others). Anthropogenic factors, on the other hand, included human activities and land use such as agriculture, mining, industry, domestic areas, landfill sites, and others (Helena et al. 2000). Further, there is another factor that influences and binds both and that is the time. The availability of groundwater to fill pores in the soil and rocks within the saturation zone is one of the essential basic concepts in groundwater chemistry (Appelo and Postma 2005). Naturally, minerals on soil or rock heavily influence the hydrochemistry of groundwater (Frape et al. 1984; Nordstrom et al. 1989; Pacheco and van der Weijden 1996; Cloutier et al. 2006; Belkhirri et al. 2011). The contact between groundwater and minerals produces chemical reactions between the two in the form of ion transfer (Domenico and Schwartz 1998; Edmunds and Shand 2008). In accordance with the laws governing chemical equilibrium, the transfer of ions will continue until equilibrium is reached (Domenico and Schwartz 1998; Appelo and Postma 2005).

Kulonprogo area, located on Java Island, Indonesia, has several landform units. Adjii and Sejati (2014) described the southern region of Kulonprogo in terms of several diverse landforms: denudational hills, denudational hillslopes, alluvial plains, natural levees, fluvio-marine plains, beaches, and beach ridges, as well as sand dunes. Also, Santosa (2012) explained the differences in observed hydrogeochemical processes within the coastal landform areas of Kulonprogo as being a result of genesis and the depositional environment in that region. In addition, the geological formations in the southern area of Kulonprogo play a role in the distribution of minerals and rocks, including breccias, sandstone, limestone, tuff, agglomerate, loam, sand, silt, and clay (van Bemmelen 1949). The consequences of complex geological and geomorphological configurations in the region have thus caused variations in the aquifer minerals, including their types, physical properties, and chemical properties. Therefore, for that matter, this research was conducted in one of the southern Kulonprogo segments composed of diverse geomorphology and geological settings, namely denudational, fluvial, aeolian, and marine landforms that lain on Old-andesite and Sentolo formation.

Groundwater movement through the porous materials and rocks in the aquifers and close contact with the minerals provides information regarding the hydrochemical processes that take place in the studied area. Adjii and Widyastuti (2005) have made reconstructions of groundwater movement in the studied area, by measuring the hydraulic head through the observation well/borehole. The set of 96 measurement point data was then interpolated to produce a groundwater contour map. In general, groundwater in the southern part of Kulonprogo, which became the studied area in this research, moves from the north (hilly area) to the south (coastal area)—through diverse landforms. Although the hydraulic head is not always correlated with relief, it can be said that the movement of groundwater in this area follows the slope of the relief. Theoretically, in a region that has diverse landforms, there will be a change in the chemical constituents of groundwater in a segment or corridor of groundwater flow. The study of hydrogeochemical changes along the flow path in the study area helps determine the relationship between landforms and the hydrogeochemistry of groundwater.

Therefore, the purpose of this study is to identify and quantify the hydrochemical processes responsible for changing the facies of hydrogeochemistry in the landform units in the studied area, namely the southern Kulonprogo region. Moreover, this research also focuses on geomorphological and hydrogeological fusion in determining hydrogeochemical characteristics based on geomorphological unit scale. Delineation based on geomorphological

units is expected to be able to become a big database and powerful tool—covering hydrological, geological, lithological, and other aspects—for further research.

2 Site Description

The study area is located in the Kokap and Temon subdistricts of southern Kulonprogo, at latitudes between 7° 51' 07" S and 7° 54' 57" S and longitudes between 110° 02' 51" E and 110° 06' 01" E. The study area covers 2412 km² between the hilly area (north) and the coastal area (south). The study area's altitude ranges from sea level up to 2150 m. The studied area is bounded by Serang River on the east side and Bogowonto River on the west side, both of which empty into the Indian Ocean (Fig. 1). The study area is included in the Serang watershed having dendritic patterns. MacDonal and Partners (1984) explained that the hydrogeological systems at this location belong to the Water Aquifer System (WAS) and the Sand Dune Aquifer System (SDAS). The WAS consists of loose sand, gravel, clay, and fluvial clay, while the SDAS consists of fine- to medium-sized sand and loam. Both aquifers have a moderate level of aquifer productivity with hydraulic conductivities of up to 5 l/s. Meanwhile, the northern part of the study area includes the hilly area of

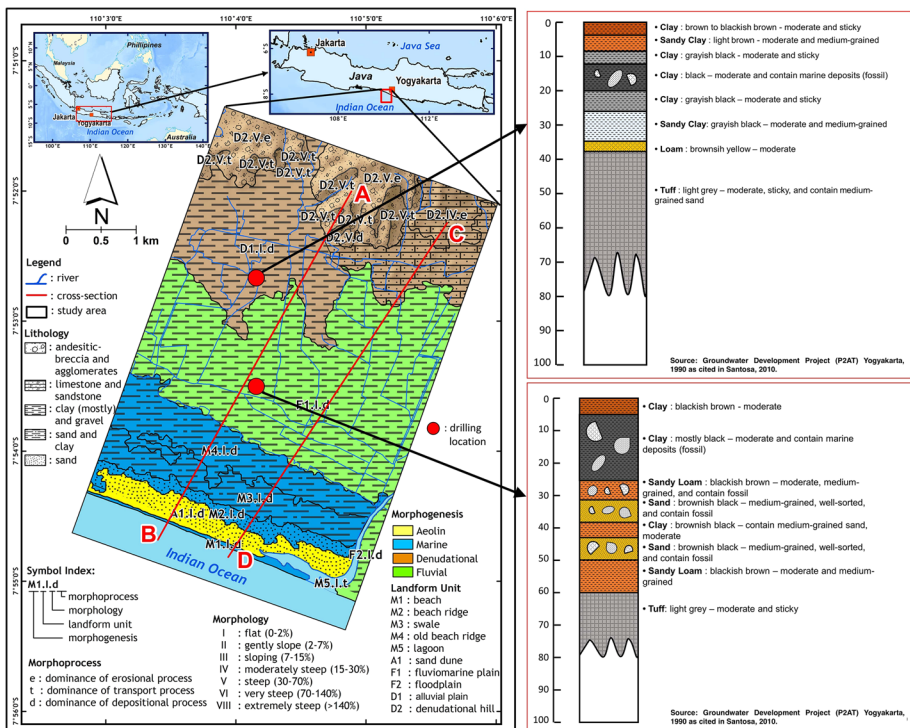


Fig. 1 Location and geomorphological map of the study area in Kulonprogo, Java, Indonesia. It consists of four landforms based on its genesis (distinguished on the map based on color symbol)—detailed information of each landform represented by the symbol index (slope classification refers to the slope classification from Van Zuidam 1983). The lines A, B represent the cross section in Fig. 4 and C, D represent the cross section in Fig. 5

Sentolo formation (SF) and the Old-andesite formation (OAF), both of which are categorized as non-aquifers. Meteorological data between 2003 and 2016 show that the average annual rainfall in the study location was 2167.9 mm/year, with a peak in the rainy season of 386.7 mm/month, in December. The rainy season (defined as the intensity of more than 100 mm/month) lasts from October to April. The average annual temperature was 27.1 °C, with the highest temperatures in October and the lowest in July.

2.1 Geology

Kulonprogo is in southern central Java. It contains the Kulonprogo hills, which have elongated domes oriented from north to south. The hills are 64 km long (north–south) and 40 km wide (west–east). The hills are referred to as an “Oblong Dome” (van Bemmelen 1949). The regional tectonic patterns, namely Sunda, Meratus, and Javanese, are controlling the structure of the hills (Syafri et al. 2013). Widagdo et al. (2018) also explain that the “oblong dome” is composed of three ancient andesite volcanoes, including the Gadjah Volcano (the oldest volcano, located in the center of the dome), the Idjo Volcano (which is toward the south of the dome), and the youngest, the Menoreh Volcano (located north of the dome). These ancient andesite volcanoes have eroded into the form of a plateau with a relatively flat top and steep slopes. As a consequence, van Bemmelen (1949) classified the northern part of the study area as the Old-andesite formation from the Upper Oligocene, with the lithology of volcanic breccia with andesite fragments, tuff, lapilli breccia, insertion of andesite lava, agglomerates, and volcanic sandstone.

Furthermore, the Kulonprogo hills complex also experienced a period of inundation during the Miocene period, which led to the development of a new formation known as the Sentolo formation (Kadar 1975). This formation is formed from a shallow sea deposition environment located non-conformably above the Old-andesite formation and the Jonggrangan formation. Based on observations from planktonic foraminifera, Harsono (1968) estimated that the Sentolo formation was formed around in the Miocene or Pliocene. The Sentolo formation is located east and southeast of the Kulonprogo hills and contains way to steep hills. The Sentolo formation is composed of sandstone, marl, and limestone conglomerates, which indicate a deeper neritic zone.

2.2 Geomorphology

Based on the genesis, the landforms in the study area can be grouped into four geomorphological groups, namely denudational, fluvial, marine, and aeolian (Fig. 1).

2.2.1 Denudational (Denudational Hills and Denudational Hillslope)

The denudational hills in the study area are divided into two units, the denudational hills of the Old-andesite formation and the denudational hills of the Sentolo formation. The terminology is based on the dominant process at work, namely mass wasting (Hadmoko et al. 2010). Additional evidence that confirms that the hills in the study segment are included in the form of denudational land comes in the form of dendritic-shaped river patterns, intensive erosion and landslide processes, and the parent rocks that are exposed.

The denudational hills of the Old-andesite formation are located in the northwest part of the study area and have a lithology of andesite breccia and agglomerates, while the denudational hills of the Sentolo formation are located in the northeastern part of

the study segment and have a marl limestone lithology. The hills have steep morphology with slope rates from 30 to 70%. Eroded or transported materials from the denudational hills are deposited to the lower part (in the south), forming denudational hillslope and alluvial plains. Meanwhile, denudational hillslope located at the south of the denudational hillsides has slope rates from 8 to 25% within a relatively narrow area. Denudational hillslope is divided into two units, namely “hillslope denudational,” composed of material from the Old-andesite formation, and “denudational hillslope,” material from the Sentolo formation. In this area, rock outcrops are rarely found because deposits from the upper slope have covered them.

2.2.2 Fluvial (Alluvial Plains and Fluviomarine Plains)

The fluvial landform in the study area is divided into two parts, namely the alluvial plain and the fluviomarine plain. They are deposited non-conformably with rock layers, which are generally older. Morphologically, Adji and Sejati (2014) described these units as flat with a slope from 0 to 3%. The composition of materials in these units, sourced during a period of fluvial deposition, is a mixture of gravel, sand, mud, and clay. The material is transported via the river and deposited laterally. By definition, an alluvial plain lies beneath denudational hills and denudational hillslopes, while a fluviomarine plain is located to the south of an alluvial plain. Santosa (2012) explained that the terminology used for a fluviomarine plain is based on its genesis within a marine depositional environment following the discovery of marine clay deposits, fossils of shallow marine molluscs, and brackish, or even salt, water that was trapped in this area.

2.2.3 Aeolian (Sand Dune)

The aeolian landform found in the research area is of the sand dune type, composed of fine-to-rough sand. Sand dune is a topographic formation formed by sand deposits transported by the wind (King 1972; Sunarto 2014). The material is loose and formed from transportation by fluvial energy emptying into the sea, from marine energy deposited on the coast, and from wind force (aeolian) forming the sand dune.

2.2.4 Marine (Beach Ridge, Swale, and Beach)

The marine landform types in the study area include beach ridge, swale, and beach. The beach ridges are divided into two forms, namely old-beach ridge and young-beach ridge, and between them is a swale. The swale is a former lagoon and back-swamp where the dominant materials are clay or fine sand. The clay layer in this landform is the result of the weathering of silicate minerals, such as orthoclase and quartz that also found in the denudational and alluvial plain of Old-andesite formation. Also, as a result of the decay of vegetation in ancient lagoons, peat is also found in the deeper layer. The beach type in this area is formed by wave processes working on clastic materials such as sand. The clastic material in this landform is a fine-grained to coarse sand material with a lot of iron ore content. Iron ore minerals in the form of wustite give the impression of dark color on the beach.

3 Materials and Methods

The two important sources of data during this research were flownets and landform maps. Flownets and the distribution of landforms were used to determine the location when sampling the groundwater for hydrogeochemical analysis. Reconstruction of the flownets was carried out by measuring groundwater levels (hydraulic head) in 107 observation wells and boreholes scattered evenly throughout the study area in late 2017. The dataset was then interpolated using three-point problem method to create equipotential lines (groundwater contour) and its flowlines (Richardson et al. 1992; Winter et al. 1998; Todd and Mays 2005; Kresic 2006). The flowlines from groundwater contour map then generated important information to determine the flow path for this research. In general, groundwater movement patterns based on hydraulic head data (in this research) are not much different from the research conducted by Adji and Widyastuti (2005).

Landform mapping was created by interpreting topographic data (Shuttle Radar Topography Mission), geology map, and remote sensing imagery—satellite imagery from Sentinel-2 and Aerial Photography using Unmanned Aerial Vehicles (Phantom, DJI, China) taken on December 17, 2017. The three types of data were then overlaid and delineated in several stages: (1) global delineation to distinguish the appearance of mountains, hills, and plains; (2) delineation based on second-order relief, to divide the units based on origin, for example, whether volcanic or structural processes; (3) delineation based on third-order relief, to highlight fluvial, glacial, solitary, marine, aeolian, organic, and denudational landscapes; (4) delineation based on fourth-order relief, by division according to formation elements or attributes such as residual, erosional, and depositional processes; (5) delineation of slopes using the van Zuidam (1983) classification; (6) delineation based on the lithology and materials (as a detail attribute). The symbol associated with each landform unit refers to the ITC classification according to the color of the landform genesis (van Zuidam 1985).

The sample points were determined from the direction of groundwater flow and the distribution of landforms. There were twelve sampled wells in this study representing each landform unit and the flow path (Fig. 2). Groundwater samples were stored in a cleansed and sterilized polyethene bottle. Observation wells were pumped for a specific time to reach the actual groundwater storage area before being sampled. As is presented in Table 1, the pumping took 12–25 min to get the actual groundwater (shown by stable the psycho-chemical parameters) with a pumping debit around 25–30 l/min.

Groundwater samples were directly measured in the field according to pH, electrical conductivity (EC), total dissolved solids (TDS), and temperature using a portable water checker (HI 98130, Hanna, USA) for EC, pH, and temperature. Also, the EDTA field titration method (1.11,110.0001 and 1.11,109.0001, Merck, Darmstadt, Germany) was used to obtain values for Ca^{2+} and HCO_3^- ions, while other ions were analyzed in the laboratory: the volumetric method was used for Mg^{2+} and SO_4^{2-} , the flame photometry method for Na^+ and K^+ , the titration method using AgNO_3 for Cl^- , the spectrophotometric method for NO_3^- , the inductively coupled plasma (ICP) method for Mn^{2+} , Al^{3+} , and Si^{4+} , and finally, atomic absorption spectroscopy (AAS) for $\text{Fe}_{(\text{tot})}$. All laboratory tests complied with the APHA 2012 and Indonesian National Standard (SNI-2009) procedures. Besides, standard methods in the field also refer to Nielsen and Nielsen (2006). Samples of the cations were acidified to $\text{pH} < 2$ with HNO_3^- . All samples were stored in a cool box with dry ice to keep the temperature close to 4 °C. All water samples were directly placed and tested in the laboratory.

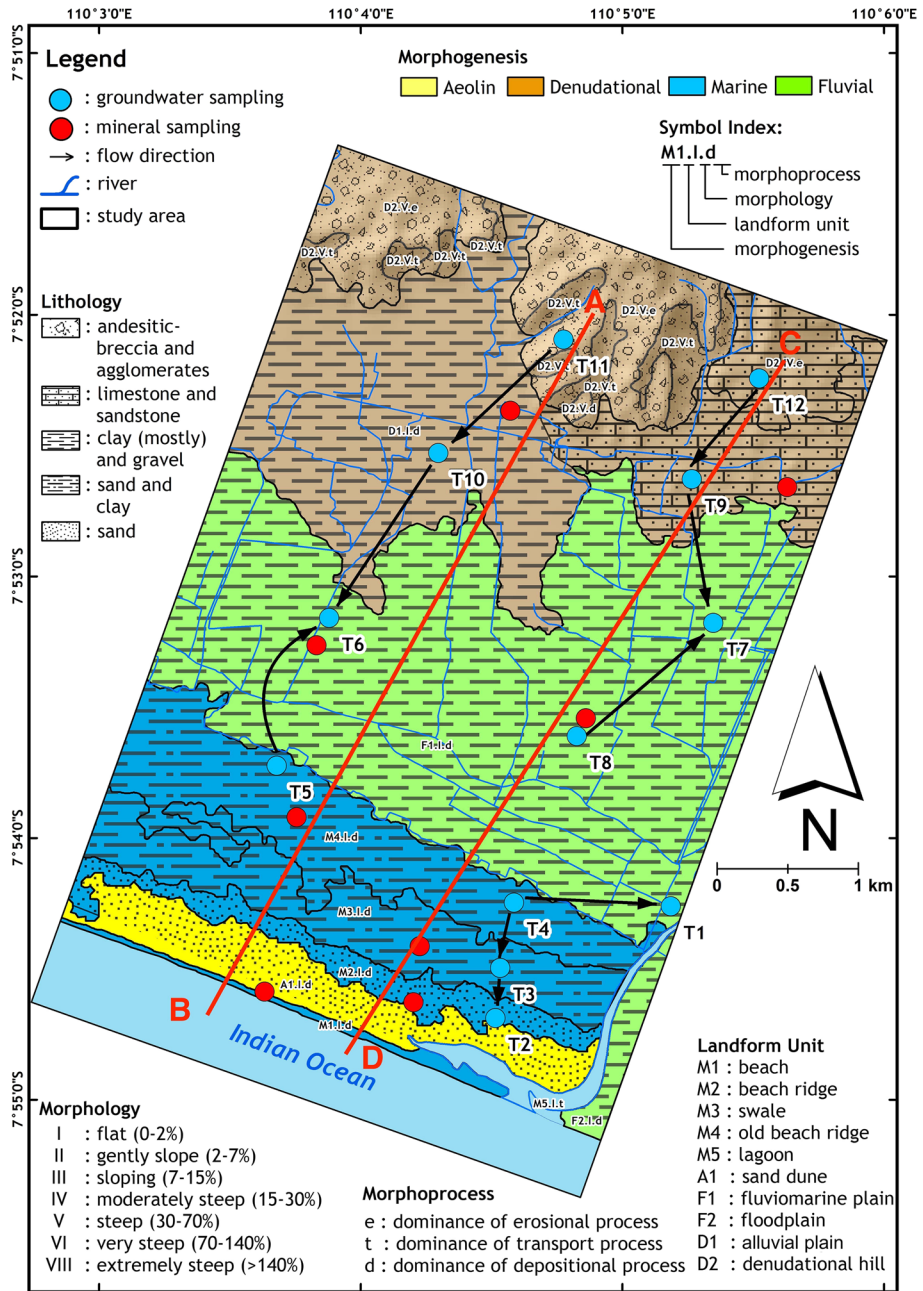


Fig. 2 Flow path map shows three observed flow paths in this research (T11–T5; T12–T8; and T1–T2). There are two major directions of groundwater flow, i.e., north to south (hilly area—fluvio-marine plain; old-beach ridges—beach) and south to north (old-beach ridges to fluvio-marine plain). Both mineral and groundwater sampling carried out in each landform

Table 1 The length of pumping time based on observation parameters to obtain actual groundwater storage

Code	Landforms	Pump- ing time (min)	Observed parameters ^a			
			pH	EC (μS/cm)	TDS (mg/l)	Tem- perature (°C)
T11	Denudational hill (West)	15	6.74	417	285	28.5
T10	Alluvial plain (West)	12	6.82	472	333	29.2
T6	Fluviomarine plain (West)	17	6.90	719	505	28.2
T5	Old-beach ridge (West)	20	6.98	1083	762	27.3
T12	Denudational hill (East)	12	7.12	528	417	31.7
T9	Alluvial plain (East)	13	7.28	785	547	28.2
T7	Fluviomarine plain (confluence point)	12	7.14	1070	751	27.6
T8	Fluviomarine plain	21	7.84	885	622	27.1
T1	Fluviomarine plain	13	7.37	356	248	27.9
T4	Old-beach ridge	20	7.64	208	143	28.0
T3	Swale	23	8.17	272	191	29.9
T2	Young-beach ridge and sand dune complex	25	8.57	275	190	28.9

^aThe values of the parameters observed were recorded under the original conditions in the field. The final value was justified when the value has stabilized for at least three times in a row

The results of the hydrochemical analysis were calculated with the charge balance error (CBE) formula to know the accuracy or rate of equilibrium deviation. The CBE formula is as follows:

$$E = [(\sum mc - \sum ma) / (\sum mc + \sum ma)] \times 100\% \tag{1}$$

where *E* is the rate of equilibrium deviation in percent (%); $\sum mc$ is the cation total in meq/l, and $\sum ma$ is the anion total in meq/l. Hiscock and Bense (2014) proposed that the maximum acceptable percentage rate of equilibrium deviation was 5%, though up to 10% can still be tolerated. The hydrochemical data of each sample are shown in Table 2.

Samples of rocks and materials were taken from every landform unit between two sample well points (Fig. 2) using a portable drill device with a drilling depth of circa 1.5 m through a mini-pit and/or directly from an outcrop using a geological hammer. Samples were then tested using the X-ray diffraction (XRD) method (SmartLab, Rigaku, Japan) to determine the minerals contained in each sample. The XRD formula to interpret the diagrams is:

$$n \lambda = 2 d \sin \theta \tag{2}$$

where *n* is diffraction order (1), λ is the wavelength, *d* is the thickness of the unit cell, and θ is the diffraction angle. The value of *d* calculated from the formula is the key to interpreting the results and determining the minerals within each sample. Figure 3 shows the result of XRD analysis in observed landforms. The interpreted result was then calibrated by the petrographic thin section method conducted by Adji and Widyastuti (2005).

Groundwater facies was classified by using the Kurlov method. Kurlov determines the facies based on its anion and cation concentrations—beyond 25% of the total ion content in meq/l (Zaporozec 1972). For mapping (symbology) purposes, the hydrogeochemical facies

Table 2 Hydrogeochemical data of groundwater samples (in ppm)

Nos.	Landform	Ca ²⁺	Mg ²⁺	Na ⁺	K ⁺	Cl ⁻	SO ₄ ²⁻	HCO ₃ ⁻	Al ³⁺	Mn ²⁺	NO ₃ ⁻	Fe _(total)	SiO ₂	CBE
T1	Fluviomarine plain	26.4	6.3	26	3	9.5	73	109.8	2.194	0.098	1.83	1.095	11.19	- 6.07
T2	Young-beach ridge & sand dune	20.8	1.9	21	7	6.0	16	97.6	0.645	0.000	7.95	0.087	22.53	- 6.11
T3	Swale	21.6	2.9	17	1	7.0	30	61.0	0.214	0.000	9.05	0.016	22.38	- 7.89
T4	Old-beach ridge (East)	9.6	3.4	26	5	6.5	17	79.3	0.307	0.004	0.28	0.106	27.85	4.99
T5	Old-beach ridge (West)	56.8	30.6	61	63	122.0	103	237.9	0.000	0.082	9.77	0.177	23.57	- 2.83
T6	Fluviomarine plain	68.0	9.7	62	3	39.0	47	305.0	0.068	0.280	0.40	0.910	16.08	- 0.86
T7	Fluviomarine plain	69.6	22.8	122	18	83.0	77	347.7	0.059	0.033	2.91	0.052	22.05	6.09
T8	Fluviomarine plain	58.4	16.0	108	6	51.0	28	433.1	0.000	0.104	0.23	0.034	16.36	- 0.26
T9	Alluvial plain (East)	101.6	4.9	34	1	50.0	21	378.2	0.133	0.009	5.60	0.028	12.74	- 9.43
T10	Alluvial plain (West)	43.2	17.0	24	8	5.5	20	237.9	0.000	0.000	0.08	0.082	25.87	3.53
T11	Denudational hill (West)	41.6	10.7	23	6	12.5	16	189.1	0.166	0.078	1.87	0.034	21.79	2.64
T12	Denudational hill (East)	57.6	15.1	24	0.31	12.0	10	252.3	0.038	0.090	0.42	0.010	21.74	4.68

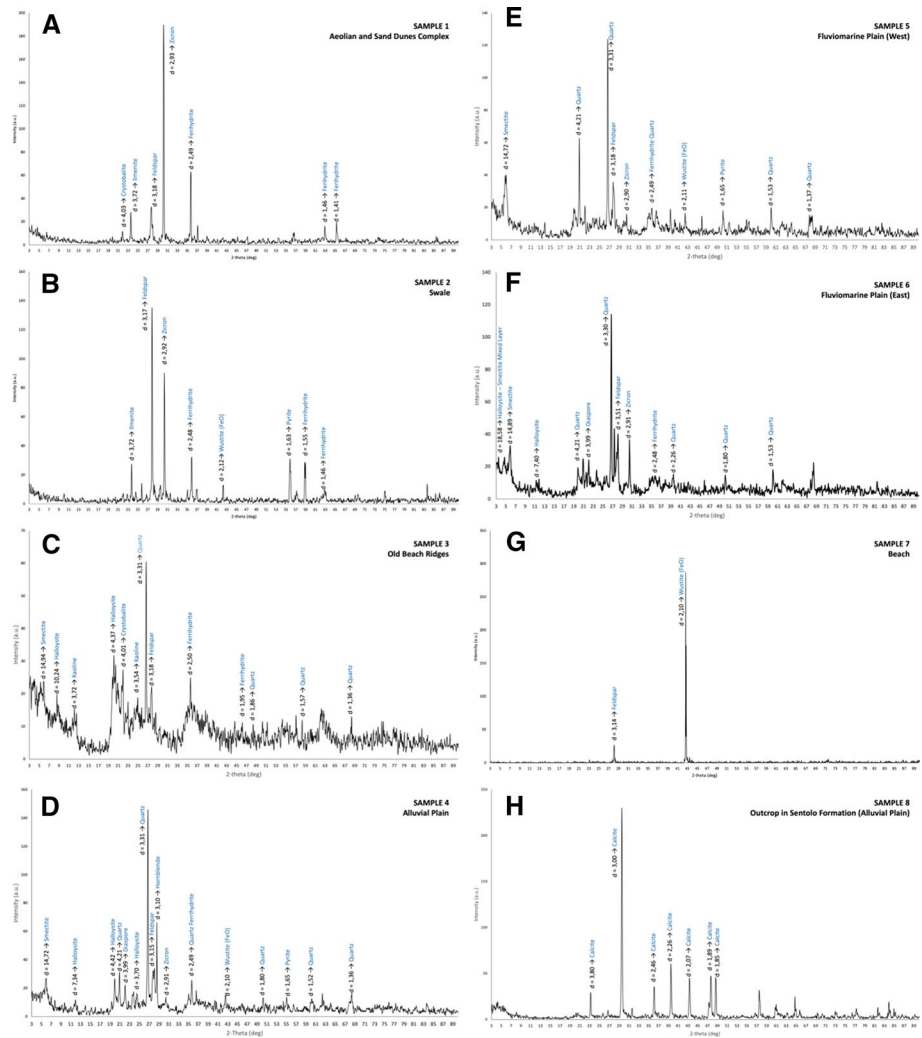


Fig. 3 XRD graph in observed landforms, from upper left to lower: **a** aeolian and sand dune complex, **b** swale, **c** old-beach ridges, **d** alluvial plain; then from upper right to lower: **e** west fluvio-marine, **f** east fluvio-marine, **g** beach, and **h** outcrop that found in west alluvial plain in Sentolo Formation

could be reported in the form of a fraction (for mapping symbol), with anion content in the numerator and cation content in the denominator. TDS information was placed before the fraction with an “M” symbol (standing for “mineralization”). In contrast, additional information such as temperature (*T*), electrical conductivity (EC), and pH, is located after the fraction. The hydrochemistry data were also plotted in the Durov diagram. This diagram could determine the facies and provide the initial guess of the occurred hydrogeochemical process—by observing the plot trendline in a flow (Chilingar 1956; Lloyd and Heathcote 1985; Younger 2007). The upper triangle is plot location for cation, while the left triangle for the anion. The unit for the chemical constituent in this diagram is meq/l. The middle

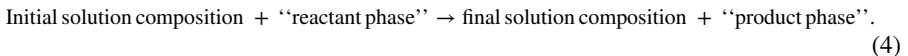
square is the place of the intersection point between two plots from the triangles, and it becomes the main object to interpret the result. Two additional boxes, in the lower and right side, provide information such as pH and total dissolved solids.

Through a knowledge of the thermodynamic tendency of each solution for dissolving or precipitating minerals (Alpers and Nordstrom 1999; Nourtier-Mazauric et al. 2005), saturation indices (SI) can be used to determine the conditions of minerals in the groundwater. The value of the SI can also determine the current status of any ongoing process or reaction using the formula:

$$SI = \log (IAP/KSP) \quad (3)$$

where SI is the saturation index, IAP is a condition that is a non-equilibrium state between reacted elements, and KSP is a mineral equilibrium constant. If the SI is positive, it indicates supersaturation with the mineral tending to precipitate out from the solution. On the other hand, a negative SI indicates undersaturation and the tendency of the solution (water) to dissolve the minerals. Equally, an SI value of zero indicates apparent equilibrium.

Furthermore, the mass balance reaction was used to determine the mass balance of minerals that either dissolved or precipitated in the flow path between the initial point and the final point. This type of modeling is also called inverse modeling (Plummer et al. 1983; Alpers and Nordstrom 1999; Adji and Widayastuti 2005; Kresic 2006). Inverse modeling is a quantitative approach that can calculate mass transfer or mass balance as a result of contact between mineral and groundwater (water–rock interaction). The principle of mass balance is:



Calculation of inverse modeling was assisted by the software programs NETPATH (Plummer et al. 1991; El-Kadi et al. 2011) and/or PHREEQC interactive codes (Parkhurst and Appelo 1999). The programs could be used to find the mass transfer from ions that have reacted from upstream to downstream or from the initial point to the final point. The data needed in mass equilibrium analysis are mineral and groundwater chemical constituents. Inverse modeling sometimes provides a lot of possible results. If this happened, the selection of the models resulted from inverse modeling is determined by the net of the hydrochemical constituent of two observed points and matching it from the saturation indices data. In this research, inverse modeling is not only for calculating the magnitude of saturation indices and mass transfer but also as verification to Durov diagram—in terms of the possible hydrogeochemical process that occurred in an observed point.

4 Results and Discussion

4.1 Hydrogeochemical Facies using Kurlov Method

Figures 4 and 5 show the cross section of landforms at flow path 1 and flow path 2, while Table 3 shows the hydrogeochemical characteristics based on a Kurlov classification. Three flow paths became the focus of interest in this research.

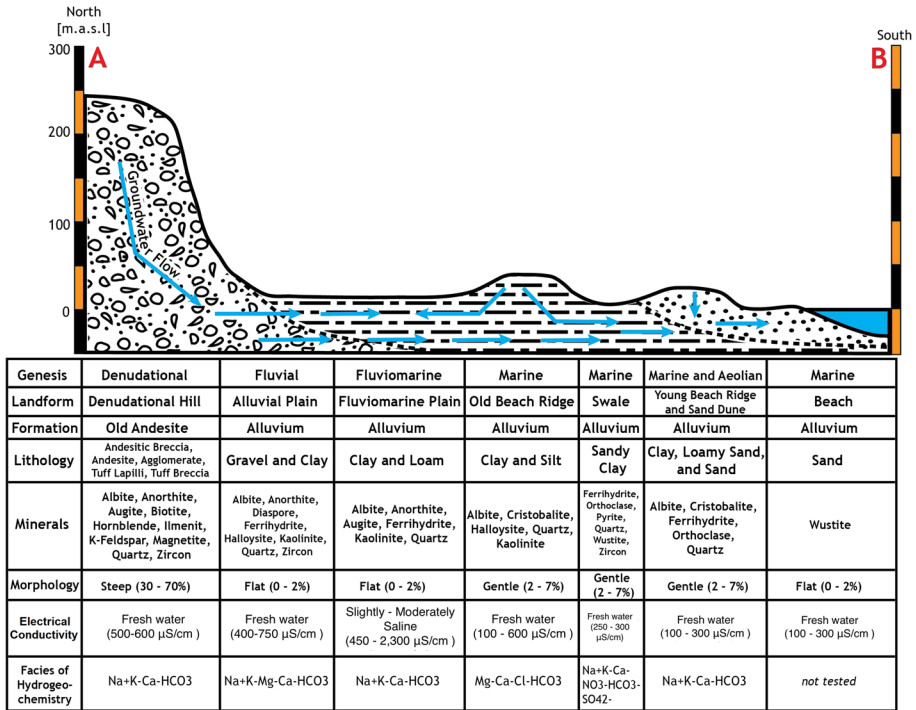


Fig. 4 Cross section of landforms attribute in flow path 1 (the location of the cross sections and their view direction are shown in Fig. 1)

- The first started on the western side, with an initial point located on the denudational hill of the Old-andesite formation and the west beach ridge, and a final point on the fluviomarine plain;
- The second flow was located in the eastern side, with an initial point on the denudational hill of the Sentolo formation and the south-eastern fluviomarine plain, and final point on the middle fluviomarine plain which became a confluence of the discharge in this flow;
- The third flow was located in the southern part of the study area where the initial point was on the old-beach ridge with two final points, namely in the eastern side of the fluviomarine plain and the young-beach ridge, and the sand dune complex (Fig. 2).

4.1.1 Flow Path 1

Groundwater in the denudational hills of the Old-andesite formation (T11) is included in the alkali–calcium–bicarbonate facies ($\text{Na}^+ + \text{K}^+ - \text{Ca}^{2+} - \text{HCO}_3^-$) and changes to magnesium–calcium–bicarbonate alkali ($\text{Na}^+ + \text{K}^+ - \text{Mg}^{2+} - \text{Ca}^{2+} - \text{HCO}_3^-$) in the western alluvial plain (T10). The Mg^{2+} increased significantly in the west of alluvial plain (T10) due to the mineral influence from the weathered Old-andesite material (augite, biotite, and hornblende). Groundwater from the western alluvial plain to the fluviomarine plain (T6) also experienced facies changes into calcium–bicarbonate alkali ($\text{Na}^+ + \text{K}^+ - \text{Ca}^{2+} - \text{HCO}_3^-$). In this landform, there was a significant increase in Na^+ and

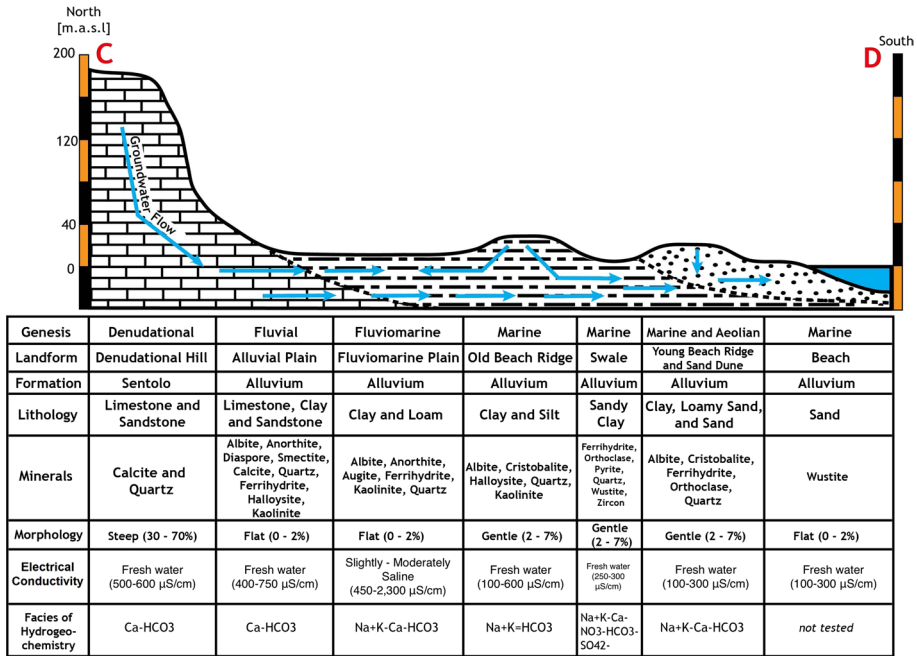


Fig. 5 Cross section of landforms attribute in flow path 2 (the location of the cross sections and their view direction are shown in Fig. 1)

Table 3 Hydrogeochemical facies at the observation point based on the Kurlov classification

No. of samples	Landform units	Kurlov classification
<i>Flow 1</i>		
T11.	Denudational hill (West)	Alkali–calcium–bicarbonate
T10.	Alluvial plain (Barat)	Alkali–magnesium–calcium–bicarbonate
T6.	Fluviomarine plain	Alkali–calcium–bicarbonate
T5.	Old-beach ridge (West)	Alkali–magnesium–calcium–chloride–bicarbonate
<i>Flow 2</i>		
T12.	Denudational hill (East)	Calcium–bicarbonate
T9.	Alluvial plain (East)	Calcium–bicarbonate
T7.	Fluviomarine plain	Alkali–calcium–bicarbonate
T8.	Fluviomarine plain	Alkali–calcium–bicarbonate
<i>Flow 3</i>		
T1.	Fluviomarine plain	Alkali–calcium–bicarbonate–sulfate
T4.	Old-beach ridge (East)	Alkali–bicarbonate
T3.	Swale	Alkali–calcium–nitrate–bicarbonate–sulfate
T2.	Young-beach ridge and sand dune complex	Alkali–calcium–bicarbonate

was followed by Ca^{2+} , all anions, and metals except for K^+ and Mg^{2+} . The groundwater in the old-beach ridge (T5), with facies of alkali–magnesium–calcium–chloride–bicarbonate ($\text{Na}^+ + \text{K}^+ - \text{Mg}^{2+} - \text{Ca}^{2+} - \text{Cl}^- - \text{HCO}_3^-$) also changed when it went through to the fluvio-marine plain (T6), showing there was a decrease in the Mg^{2+} and Cl^- dominance.

4.1.2 Flow Path 2

The denudational hills of the Sentolo formation (T12) are characterized by calcium–bicarbonate ($\text{Ca}^{2+} - \text{HCO}_3^-$) facies. The content of Ca^{2+} and HCO_3^- in this unit was very high (above 50%) because it was composed of limestone and sandstone dominated by calcite minerals. Based on the conceptual model created by Blanchette et al. (2010), groundwater in T12 and T9 is included in phase one so that Ca^{2+} and HCO_3^- content at these points becomes the major content. The calcite dissolution process will be investigated and explained in the saturation indices and inverse modeling section. Apart from fluctuations in the dissolved ion content, groundwater in the eastern alluvial plain (T9) did not undergo the evolution or changes in the hydrogeochemical facies from the recharge region and was also characterized by the calcium–bicarbonate facies ($\text{Ca}^{2+} - \text{HCO}_3^-$). This revealed that there was a strong influence from the recharge area, which contained a predominance of calcite minerals. In addition, the hydrochemical facies of the second stream experienced significant changes when passing through the eastern fluvio-marine plain (T7 and T8). These changes were characterized by alkali–calcium–bicarbonate facies ($\text{Na}^+ + \text{K}^+ - \text{Ca}^{2+} - \text{HCO}_3^-$). The increase in Na^+ and K^+ in this unit highlighted the abundance of clay minerals.

4.1.3 Flow Path 3

The old-beach ridge in the eastern part of the study area (T4) contains alkali–bicarbonate facies ($\text{Na}^+ + \text{K}^+ - \text{HCO}_3^-$). This was characterized by the relatively high (more than 50%) percentage of HCO_3^- . That indicates that any rainwater that fell as recharge in this area did not experience advanced hydrogeochemical processes. This was supported by the relatively low concentration of TDS. Furthermore, from the eastern old-beach ridge (T4), groundwater facies changed into alkali–calcium–bicarbonate–sulfate ($\text{Na}^+ + \text{K}^+ - \text{Ca}^{2+} - \text{HCO}_3^- - \text{SO}_4^{2-}$) facies in the southern fluvio-marine plain (T1) and alkali–calcium–nitrate–bicarbonate–sulfate ($\text{Na}^+ + \text{K}^+ - \text{Ca}^{2+} - \text{NO}_3^- - \text{HCO}_3^- - \text{SO}_4^{2-}$) facies in the swale (T3). The groundwater facies in the swale (T3) was the most complex when compared to the other units owing to an increasing concentration of Ca^{2+} , NO_3^- , and SO_4^{2-} . The SO_4^{2-} concentration was associated with the presence of pyrite, the result of the decay of organic matter in the past.

Meanwhile, Ca^{2+} and SO_4^{2-} in the southern fluvio-marine plain (T1) increased quite considerably, followed by other ions. This is thought to be due to the length of time it takes groundwater to flow down the gentler incline, as indicated by the increase in TDS values. Groundwater in young-beach ridge and the sand dunes complex (T2) had alkali–calcium–bicarbonate facies ($\text{Na}^+ + \text{K}^+ - \text{Ca}^{2+} - \text{HCO}_3^-$). A reduction in NO_3^- and SO_4^{2-} occurred significantly in this area, while HCO_3^- , Na^+ , K^+ , Al^{3+} , and $\text{Fe}_{(\text{total})}$ all increased.

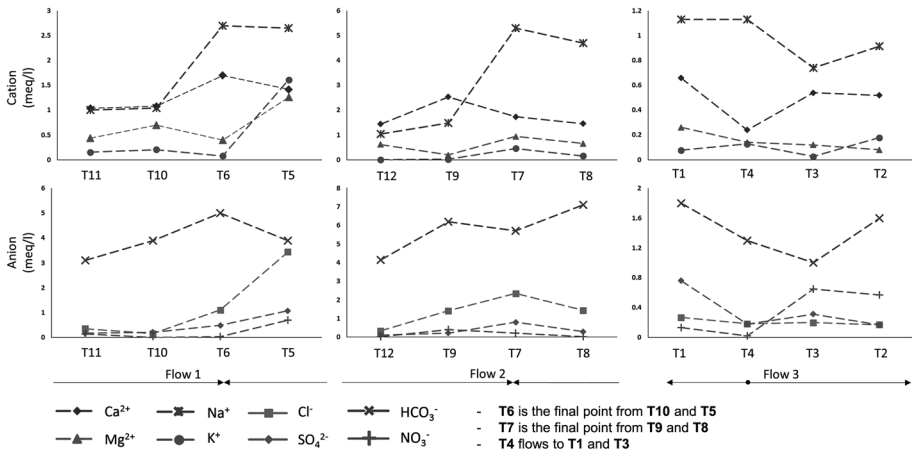


Fig. 6 Fluctuation (evolution) of groundwater chemical constituent. The upper graphs show the cation concentration, while the lower graphs show the anion concentration. X-axis informs the flow path (points), and Y-axis informs the concentration in meq/l

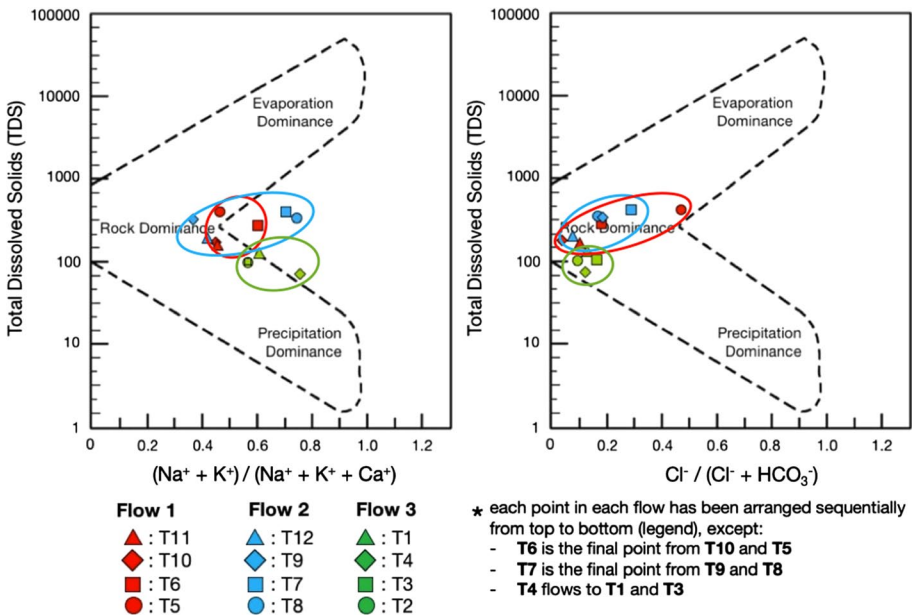


Fig. 7 Mechanism controlling groundwater chemical constituent in Gibbs curve. The chemical constituent of groundwater strongly affected by rocks (minerals)—where the dots located in the middle of the Gibbs curve. The point of each flow path represented by the colored shape and red circle represents the first flow path, the blue circle represents the second flow path, and the green circle represents the third flow path

4.2 Hydrogeochemical Characteristics

The line graph in Fig. 6 provides information about the changes of major ion in observed groundwater along flow paths. In terms of its chemical constituent, this graph authenticates the groundwater evolves from one landform to another—the changes of groundwater constituent at the study site strongly influenced by typical mineral abundance in each landform. For instance, the concentration of Ca^{2+} in the denudational hill and alluvial plain at the eastern side is more saturated than the others. It is because of the abundance of calcite from the limestone that commonly found at the Sentolo Formation. This argument is strongly supported by the Gibbs curve in Fig. 7 that shows the hydrogeochemical conditions at the study site greatly influenced by the water–rock interaction process (rock dominance). Further, it seems that this research is also supporting the thought from Blanchette et al. (2010) that stated hydrogeological and geological setting (including the mineral property that its abundance correlated with the geomorphological setting) has an impact on the chemical composition of groundwater.

Hereinafter, this curve also shows the dominance process in the flow corridor sequentially. The first and second flows that geomorphologically classified as hilly and plain area tend toward rock dominance to evaporation dominance. This could be interpreted that the groundwater in the fluvio-marine plain—as the final point of groundwater flow—is relatively old. The evaporation in this landform mostly triggered by the vegetation and loss of soil moisture by the sunlight (approximately 9–11 h per day). Luo et al. (2018) explained that most of the shallow groundwater experienced the evaporation process in their study. This is similar wherein the groundwater on this plain is relatively shallow and as a final spot of the groundwater from the northern region. Nevertheless, at the third flow (coast area), the process is quite different, where it leans to the precipitation dominance from rock dominance. Even though possibly there is an evaporation process that occurs, however, the groundwater mostly recharged directly by rainwater. It is supported by its TDS that relatively low with the tendency of precipitation dominance. This is the uniqueness of the coastal area from the standpoint of its hydrogeological characteristics—where this region is categorized as a local aquifer by MacDonald and Partner (1984) and Santosa (2012).

Next, Fig. 8 shows the hydrogeochemical characteristics based on the Durov diagram. From the figure, it can be seen that the hydrogeochemical pH characteristics in the study area indicated a relatively neutral (6.5–8.7). On the other hand, the TDS was relatively varied, from 148 to 717 mg/l. It can be revealed that physicochemical characteristics (EC and TDS) of the recharge area (denudational hills) down toward the transition-discharge area (alluvial plains and fluvio-marine plains) that experienced an upward trend. This was probably due to the residence time being longer in the transition and discharge zone compared to the groundwater in the recharge area, resulting in more intensive water–rock interaction in those areas.

To extend this argument, taking account of Darcy's law (1856), the velocity of groundwater flow in transition and discharge area is relatively slower than in the recharge area. It is mostly affected by the hydraulic gradient (∇H) which is steeper (higher) in the recharge zone, particularly in the observed area ($\nabla H_{\text{recharge}} > \nabla H_{\text{transition \& discharge}}$). Moreover, in terms of hydraulic conductivity that is a function of both the porous medium and the fluid properties (Gray and Miller 2004), the average hydraulic conductivity in the observed recharge area is relatively higher than the rest area. The average value of hydraulic conductivity (de Marsily 1986) in the recharge

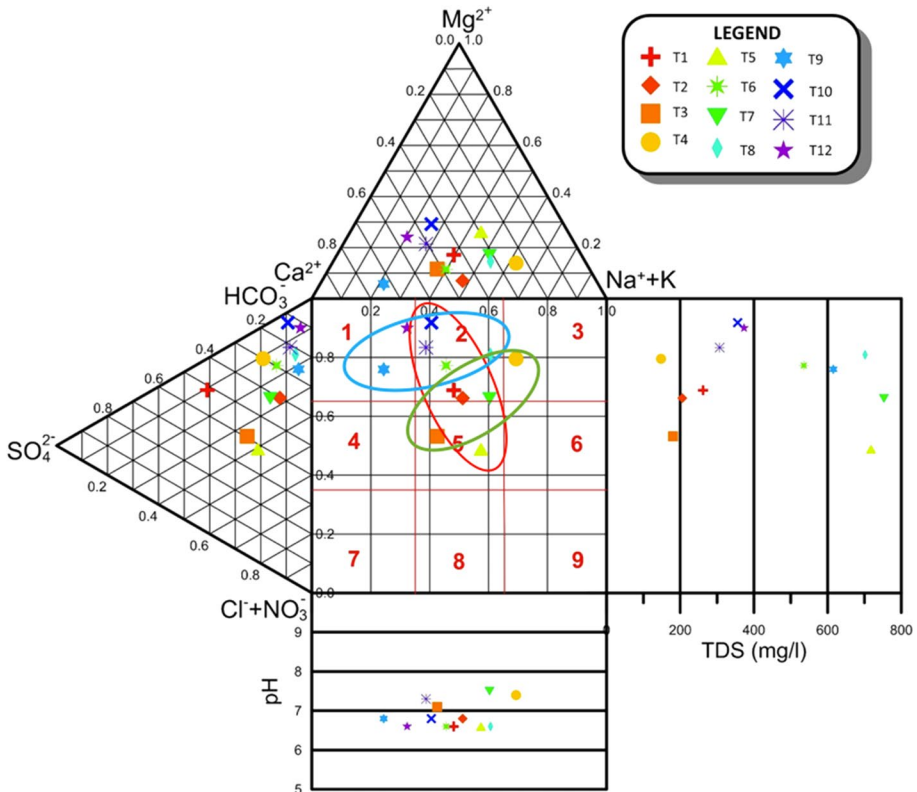


Fig. 8 Durov diagram for hydrogeochemical characteristics in the study area. The trend from the first (T11, T10, T6, and T5) and second flow (T12, T9, T7, and T8) plot points is relatively moving from the left to the right side—indicating there is an ion exchange process in these flow paths. In contrast, the third flow path (T1, T4, T3, and T2) is relatively moving from the lower right to the upper left—indicating there are reverse ion exchange and mixing processes. The red circle represents the first flow path, the blue circle represents the second flow path, and the green circle represents the third flow path

area, which mostly contains consolidated media, is from 10^{-5} to 10^{-9} m/s for the eastern part (i.e., sandstone and limestone) and 10^{-9} – 10^{-13} m/s for the western part (i.e., andesite breccia). On the other hand, for the transition and discharge that contains loam, silt, and clay, the hydraulic conductivity is from 10^{-9} to 10^{-13} . Therefore, the condition of hydraulic gradient and hydraulic conductivity associated with the residence time is affecting chemical constituent due to water–rock interaction results. Another fact, even though the hydraulic gradient in the coastal area is relatively gentle and flat, however, the value of hydraulic conductivity is quite higher than the other landforms, around 10^{-1} – 10^{-5} m/s (a mixture of sand, gravel, silt, and loess). So that, the residence time in these landforms is relatively short—due to the hydraulic conductivity—and the condition of the chemical constituent is also non-complex.

The EC of groundwater in the denudational hills of Old-andesite formation (T11) and Sentolo formation (T12) was 328 $\mu\text{S}/\text{cm}$ and 205 $\mu\text{S}/\text{cm}$, respectively. Groundwater in this area was therefore categorized as freshwater (Rhoades et al. 1992), a conclusion reinforced by the relatively low TDS levels, namely 168 mg/l and 205 mg/l. This

characteristic is typical for the recharge area. The concentration of alkali (K^+ and Na^+) and Mg^{2+} in the denudational hills of the Old-andesite formation was relatively high. On the other hand, in the denudational hills of the Sentolo formation, the Ca^{2+} and HCO_3^- levels were high. Although the locations of the two hill clusters are relatively close, the hydrogeochemical conditions of the two hills are discrete due to mineral constituent. Given that mineral is a typical attribute of a geomorphological unit, it can be said that hydrogeochemical conditions can be determined by geomorphological units. This finding shows that a delineation of an area based on its landform can provide derivative information about the quality of groundwater resources. This can be a powerful and efficient tool for regional planners, such as the government, to comprehend the condition of

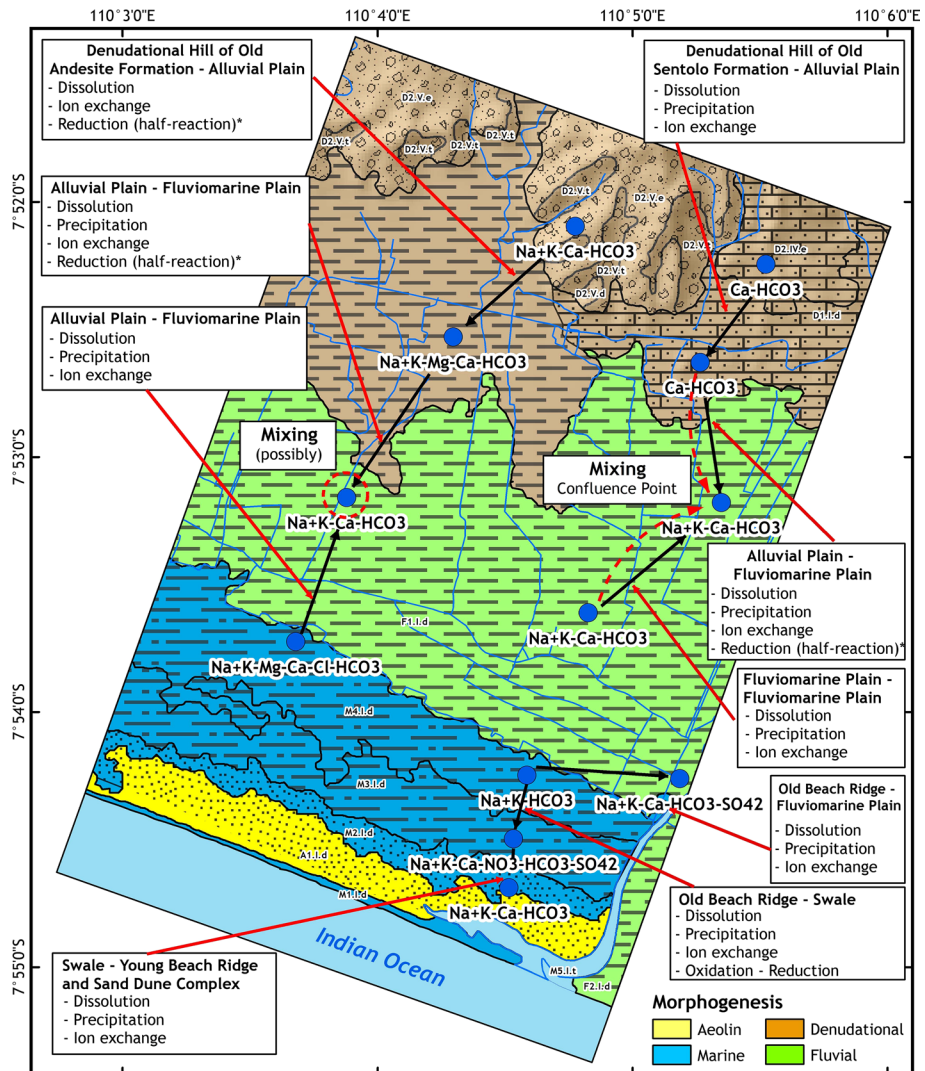


Fig. 9 Hydrogeochemical facies and their processes in the study area

Table 4 The saturation indices of minerals in each landform unit

Code	Landform units	Minerals	Chemical formula	Mineral class ^a	SI		
T11	Denudational hill (West)	Albite	$\text{NaAlSi}_3\text{O}_8$	Plagioclase (silicates)	2.19		
		Anorthite	$\text{CaAl}_2\text{Si}_2\text{O}_8$	Plagioclase (silicates)	- 1.00		
		Augite	$(\text{Ca},\text{Na})(\text{Mg},\text{Fe},\text{Al},\text{Ti})(\text{Si},\text{Al})_2\text{O}_6$	Silicates	-		
		Biotite	$\text{K}(\text{Mg},\text{Fe})_3(\text{AlSi}_3\text{O}_{10})(\text{F},\text{OH})_2$	Silicates	-		
		Hornblende	$\text{Ca}_2(\text{Mg},\text{Fe},\text{Al})_5(\text{Al},\text{Si})_8\text{O}_{22}(\text{OH})_2$	Silicates	-		
		Ilmenite	FeTiO_3	Oxides and hydroxides	-		
		K-feldspar	KAIS_3O_8	Silicates	1.82		
		Magnetite	Fe_3O_4 or $\text{Fe}_2\text{H}_2\text{O}_4$	Oxides and hydroxides	5.82		
		Quartz	SiO_2	Silicates	0.85		
		Zircon	ZrSiO_4	Silicates	-		
		T10	Alluvial plain (West)	Albite	$\text{NaAlSi}_3\text{O}_8$	Plagioclase (silicates)	-
				Anorthite	$\text{CaAl}_2\text{Si}_2\text{O}_8$	Plagioclase (silicates)	-
				Diaspore	$\text{AlO}(\text{OH})$	Oxides and hydroxides	-
				Ferrhydrite	$(\text{Fe}^{3+})_2\text{O}_3 \cdot 0.5 \text{H}_2\text{O}$	Oxides and hydroxides	-
Halloysite	$\text{Al}_2\text{Si}_2\text{O}_5(\text{OH})_4$			Silicates	-		
Kaolinite	$\text{Al}_2\text{Si}_2\text{O}_5(\text{OH})_4$			Silicates	-		
Quartz	SiO_2			Silicates	-		
Wustite	FeO			Silicates	0.91		
T6	Fluviomarine plain (West)			Albite	$\text{NaAlSi}_3\text{O}_8$	Oxides and hydroxides	- 5.55
				Anorthite	$\text{CaAl}_2\text{Si}_2\text{O}_8$	Plagioclase (silicates)	1.89
		Augite	$(\text{Ca},\text{Na})(\text{Mg},\text{Fe},\text{Al},\text{Ti})(\text{Si},\text{Al})_2\text{O}_6$	Plagioclase (silicates)	- 1.78		
		Ferrhydrite	$(\text{Fe}^{3+})_2\text{O}_3 \cdot 0.5 \text{H}_2\text{O}$	Silicates	-		
		Kaolinite	$\text{Al}_2\text{Si}_2\text{O}_5(\text{OH})_4$	Oxides and hydroxides	-		
		Quartz	SiO_2	Silicates	6.89		
		Albite	$\text{NaAlSi}_3\text{O}_8$	Silicates	0.72		
				Plagioclase (silicates)	-		
T5	Old-beach ridge (West)						

Table 4 (continued)

Code	Landform units	Minerals	Chemical formula	Mineral class ^a	SI
T12	Denudational hill (East)	Cristobalite	SiO ₂	Silicates	0.36(α); – 0.08(β)
		Halloysite	Al ₂ Si ₂ O ₅ (OH) ₄	Silicates	–
		Kaolinite	Al ₂ Si ₂ O ₅ (OH) ₄	Silicates	–
		Quartz	SiO ₂	Silicates	0.91
		Biotite	K(Mg,Fe) ₃ (AlSi ₃ O ₁₀ (F,OH) ₂	Silicates	–
		Calcite	CaCO ₃	Carbonates	– 0.05
		Hornblende	Ca ₂ (Mg,Fe,Al) ₅ (Al,Si) ₈ O ₂₂ (OH) ₂	Silicates	–
		Orthoclase	KAlSi ₃ O ₈	Silicates	2.24
		Quartz	SiO ₂	Silicates	0.79
		Albite	NaAlSi ₃ O ₈	Plagioclase (silicates)	1.67
		Anorthite	CaAl ₂ Si ₂ O ₈	Plagioclase (silicates)	– 1.10
		Calcite	CaCO ₃	Carbonates	0.44
T9	Alluvial plain (East)	Diaspore	AlO(OH)	Oxides and hydroxides	2.93
		Ferrihydrite	(Fe ³⁺) ₂ O ₃ ·0.5 H ₂ O	Oxides and hydroxides	–
		Halloysite	Al ₂ Si ₂ O ₅ (OH) ₄	Silicates	6.61
		Kaolinite	Al ₂ Si ₂ O ₅ (OH) ₄	Silicates	0.62
		Quartz	SiO ₂	Silicates	– 5.63
		Wustite	FeO	Oxides and hydroxides	– 5.63
		Albite	NaAlSi ₃ O ₈	Plagioclase (silicates)	2.61
		Anorthite	CaAl ₂ Si ₂ O ₈	Plagioclase (silicates)	– 1.55
		Diaspore	AlO(OH)	Oxides and hydroxides	2.71
		Ferrihydrite	(Fe ³⁺) ₂ O ₃ ·0.5 H ₂ O	Oxides and hydroxides	–
		Halloysite	Al ₂ Si ₂ O ₅ (OH) ₄	Silicates	–
		Kaolinite	Al ₂ Si ₂ O ₅ (OH) ₄	Silicates	6.69
T7	Fluviomarine plain (confluence point)	Quartz	SiO ₂	Silicates	0.87

Table 4 (continued)

Code	Landform units	Minerals	Chemical formula	Mineral class ^a	SI		
T8	Fluviomarine plain	Albite	NaAlSi ₃ O ₈	Plagioclase (silicates)	–		
		Anorthite	CaAl ₂ Si ₂ O ₈	Plagioclase (silicates)	–		
		Diaspore	AlO(OH)	Oxides and hydroxides	–		
		Ferrihydrite	(Fe ³⁺) ₂ O ₃ ·0.5 H ₂ O	Oxides and hydroxides	–		
		Halloysite	Al ₂ Si ₂ O ₅ (OH) ₄	Silicates	–		
		Kaolinite	Al ₂ Si ₂ O ₅ (OH) ₄	Silicates	–		
		Quartz	SiO ₂	Silicates	0.75		
		Albite	NaAlSi ₃ O ₈	Plagioclase (silicates)	2.60		
		Anorthite	CaAl ₂ Si ₂ O ₈	Plagioclase (silicates)	0.60		
		Cristobalite	SiO ₂	Silicates	0.03 (α); – 0.41 (β)		
T1	Fluviomarine plain	Ferrihydrite	(Fe ³⁺) ₂ O ₃ ·0.5 H ₂ O	Oxides and hydroxides	–		
		Halloysite	Al ₂ Si ₂ O ₅ (OH) ₄	Silicates	–		
		Kaolinite	Al ₂ Si ₂ O ₅ (OH) ₄	Silicates	8.70		
		Quartz	SiO ₂	Silicates	0.57		
		Albite	NaAlSi ₃ O ₈	Plagioclase (silicates)	3.02		
		Cristobalite	SiO ₂	Silicates	0.42 (α); – 0.02 (β)		
		Halloysite	Al ₂ Si ₂ O ₅ (OH) ₄	Silicates	–		
		Kaolinite	Al ₂ Si ₂ O ₅ (OH) ₄	Silicates	7.42		
		Quartz	SiO ₂	Silicates	0.96		
		Ferrihydrite	(Fe ³⁺) ₂ O ₃ ·0.5 H ₂ O	Oxides and hydroxides	–		
T3	Swale	Orthoclase	KAlSi ₃ O ₈	Silicates	3.74		
		Pyrite	FeS ₂	Sulfides	–		
		Quartz	SiO ₂	Silicates	0.83		
		Wustite	FeO	Oxides and hydroxides	– 6.3		
		Zircon	ZrSiO ₄	Silicates	–		
		T4	Old-beach ridge	Albite	NaAlSi ₃ O ₈	Plagioclase (silicates)	–
				Cristobalite	SiO ₂	Silicates	–
				Halloysite	Al ₂ Si ₂ O ₅ (OH) ₄	Silicates	7.42
Kaolinite	Al ₂ Si ₂ O ₅ (OH) ₄			Silicates	0.96		
Quartz	SiO ₂			Silicates	–		
Ferrihydrite	(Fe ³⁺) ₂ O ₃ ·0.5 H ₂ O			Oxides and hydroxides	–		
Orthoclase	KAlSi ₃ O ₈			Silicates	3.74		
Pyrite	FeS ₂			Sulfides	–		
Quartz	SiO ₂			Silicates	0.83		
Wustite	FeO			Oxides and hydroxides	– 6.3		

Table 4 (continued)

Code	Landform units	Minerals	Chemical formula	Mineral class ^a	SI
T2	Young-beach ridge and sand dune complex	Albite Cristobalite Ferrhydrite Orthoclase Quartz	NaAlSi ₃ O ₈ SiO ₂ (Fe ³⁺) ₂ O ₃ ·0.5 H ₂ O KAlSi ₃ O ₈ SiO ₂	Plagioclase (silicates) Silicates Oxides and hydroxides Silicates Silicates	2.86 0.29(α); – 0.14(β) – 5.13 0.83

^aThe classification of minerals refers to the Dana (1949)

the region's natural resources, including hydrogeochemical conditions, through geomorphological mapping.

Groundwater in the fluvio-marine plain in T7 had a relatively high TDS and EC value—compared to the other fluvio-marine units (T1, T6, and T8)—because it was the confluence of the groundwater discharge (Figs. 2, 9). In general, the Durov diagram provides an initial conjecture of hydrogeochemical processes—qualitatively from the trend plot, namely ion exchange (on flow paths 1 and 2), reverse ion exchange (on flow path 3), and mixing, also on flow path 3. The verification of this conjecture and the calculation of the mass balance (quantitatively) will be presented in inverse modeling section.

4.3 Saturation Indices

The distribution of minerals in the aquifers and their saturation indices are presented in Table 4. Samples representing the hydrogeochemical conditions in the denudational hills were divided into two samples, namely T11 (Old-andesite on the west side) and T12 (Sentolo formation on the east). The difference between these is to do with their minerals: the Sentolo formation is dominated by carbonate minerals, whereas the Old-andesite formation is dominated by minerals from volcanic processes. This condition increases the pH in T12. Conversely, K⁺ levels in T11 are higher than in T12 because of the interaction between groundwater and K-feldspar minerals in the rock. In T12, the saturation indices of calcite minerals were still on the undersaturated (dissolution) phase.

Samples from alluvial plain units were divided into two samples, namely T10 (alluvial plain, affected by the materials from the Old-andesite formation) and T9 (alluvial plain affected by the materials from the Sentolo formation). The SiO₂ content in T10 increased compared to the recharge area (T11), probably because of the presence of other dissolved silica minerals, such as anorthite. In the eastern alluvial plain (T9), the saturation indices with respect to calcite, diaspore, and most of the silicate minerals came out as saturated. At the same time, the anorthite and wustite were still undersaturated. At this point, there was also an increasing concentration of Al³⁺ and SiO₂ due to the dissolution of anorthite (undersaturated).

Groundwater samples in the fluvio-marine plain were carried out at T6 (west fluvio-marine plain), T7 and T8 (east fluvio-marine plain), and T1 (south fluvio-marine plain). The saturation indices of fluvio-marine generally show that most of the silicate minerals, oxides, and hydroxides were supersaturated (precipitation) with regard to albite, quartz, kaolinite, cristobalite, and diaspore. Meanwhile, the anorthite (silicate) mineral was still unsaturated (dissolved). Groundwater samples in the old-beach ridge, namely T5 and T4, were dominated by silicate minerals so that the saturation indices show that most of the silicate minerals were supersaturated (precipitated). This was indicated by the relatively high level of SiO₂ in comparison with other landforms units. Groundwater from the old-beach ridge is not only flowing southward—the swale (T3) unit—but also to the fluvio-marine plain in the north. At this location, the minerals found are categorized as silicates (orthoclase, pyrite, quartz, and zircon) and oxide-hydroxide minerals (ferrihydrite and wustite). The saturation indices indicate that silicate minerals such as orthoclase and quartz were supersaturated (precipitated). The primary reasons were the high content of SiO₂ in groundwater carried away from the old-beach ridge and the dominance of silicate minerals in the swale. In comparison, oxide-hydroxide minerals such as wustite are dissolving (undersaturated).

The T2 point represents groundwater at the young-beach ridge and sand dune complex. This unit is similar to the minerals in the old-beach ridge, which are dominated by silicates

Table 5 Mass balance results along flow paths in the study area

Nos.	Flows	Minerals	Mineral reactions
1.	T11 (denudational hill of the old-andesite formation)–T10 (alluvial plain)	Halloysite Quartz Diaspore Ferrhydrite	$6.45 \times 10^{-3} \text{ Albite}_{(s)} + 2.58 \times 10^{-2} \text{ H}^{+}_{(aq)} + 3.225 \times 10^{-3} \text{ Diaspore}_{(s)} + 3.225 \times 10^{-3} \text{ Ferrhydrite}_{(s)} + 3.225 \times 10^{-3} \text{ Anorthite}_{(s)} + 3.225 \times 10^{-3} \text{ H}_2\text{CO}_{3(s)} \rightarrow 6.45 \times 10^{-3} \text{ Kaolinite/Halloysite}_{(s)} + 9.675 \times 10^{-3} \text{ Quartz}_{(s)} + 6.45 \times 10^{-3} \text{ Na}^{+}_{(aq)} + 3.225 \times 10^{-3} \text{ H}_4\text{SiO}_{4(s)} + 3.225 \times 10^{-3} \text{ Al}^{3+}_{(aq)} + 3.225 \times 10^{-3} \text{ Fe}^{3+}_{(aq)} + 6.45 \times 10^{-3} \text{ H}_2\text{O}_{(l)} + 3.225 \times 10^{-3} \text{ Ca}(\text{HCO}_3)_2(s)$
2.	T10 (alluvial plain)–T6 (fluviomarine plain)	Quartz Diaspore Ferrhydrite Quartz	$1.654 \times 10^{-3} \text{ Albite}_{(s)} + 6.2025 \times 10^{-3} \text{ H}_2\text{O}_{(l)} + 8.27 \times 10^{-4} \text{ Anorthite}_{(s)} + 8.27 \times 10^{-4} \text{ H}_2\text{CO}_{3(s)} + 8.27 \times 10^{-4} \text{ Pyrite}_{(s)} + 3.10125 \times 10^{-3} \text{ O}_{2(g)} \rightarrow 1.654 \times 10^{-3} \text{ Kaolinite/Halloysite}_{(s)} + 2.481 \times 10^{-3} \text{ Quartz}_{(s)} + 1.654 \times 10^{-3} \text{ Na}^{+}_{(aq)} + 8.27 \times 10^{-4} \text{ H}_4\text{SiO}_{4(s)} + 8.27 \times 10^{-4} \text{ Ca}(\text{HCO}_3)_2(s) + 8.27 \times 10^{-4} \text{ Ferrhydrite}_{(s)} + 1.654 \times 10^{-3} \text{ SO}^{2-}_{4(aq)} + 1.654 \times 10^{-3} \text{ H}^{+}_{(aq)}$
3.	T5 (old-beach ridge)–T6 (fluviomarine plain)	Albite Ferrhydrite Pyrite Quartz	$1.1172 \times 10^{-3} \text{ Quartz}_{(s)} + 5.586 \times 10^{-4} \text{ Na}^{+}_{(aq)} + 2.793 \times 10^{-4} \text{ Anorthite}_{(s)} + 5.586 \times 10^{-4} \text{ H}_2\text{CO}_{3(s)} + 2.793 \times 10^{-4} \text{ Ferrhydrite}_{(s)} + 2.793 \times 10^{-4} \text{ H}^{+}_{(aq)} + 5.586 \times 10^{-4} \text{ Gibbsite}_{(s)} + 5.586 \times 10^{-4} \text{ H}_4\text{SiO}_{4(s)} \rightarrow 5.586 \times 10^{-4} \text{ Albite}_{(s)} + 2.2344 \times 10^{-3} \text{ H}_2\text{O}_{(l)} + 2.793 \times 10^{-4} \text{ Ca}(\text{HCO}_3)_2(s) + 2.793 \times 10^{-4} \text{ Fe}^{3+}_{(aq)} + 2.793 \times 10^{-4} \text{ Kaolinite/Halloysite}_{(s)}$
		Albite Ferrhydrite Pyrite	

Table 5 (continued)

Nos.	Flows	Minerals	Mineral reactions
4.	T12 (denudational hill of the Sentolo formation)–T9 (alluvial plain)	Halloysite Anorthite	$6.364 \times 10^{-3} \text{H}_2\text{O}_{(l)} + 1.591 \times 10^{-3} \text{Diaspore}_{(s)} + 1.2728 \times 10^{-2} \text{H}^+_{(aq)} + 1.591 \times 10^{-3} \text{Ferrhydrite}_{(s)} + 3.182 \times 10^{-3} \text{Albite}_{(s)} + 1.591 \times 10^{-3} \text{Anorthite}_{(s)} + 1.591 \times 10^{-3} \text{H}_2\text{CO}_{3(s)} + 1.591 \times 10^{-3} \text{Wustite}_{(s)} + 1.591 \times 10^{-3} \text{Calcite}_{(s)} \rightarrow 1.591 \times 10^{-3} \text{H}_4\text{SiO}_{4(s)} + 1.591 \times 10^{-3} \text{Al}^{3+}_{(aq)} + 1.591 \times 10^{-3} \text{Fe}^{2+}_{(aq)} + 1.591 \times 10^{-3} \text{Fe}^{2+}_{(aq)} + 3.182 \times 10^{-3} \text{Gibbsite}_{(s)} + 4.773 \times 10^{-3} \text{Quartz}_{(s)} + 3.182 \times 10^{-3} \text{Na}^+_{(aq)} + 1.591 \times 10^{-3} \text{Ca}(\text{HCO}_3)_2_{(s)} + 1.591 \times 10^{-3} \text{Kaolinite/Halloysite}_{(s)} + 1.591 \times 10^{-3} \text{Ca}_{(aq)} + {}^{2+} 1.591 \times 10^{-3} \text{HCO}_3^-_{(s)} + 1.591 \times 10^{-3} \text{OH}^-_{(aq)}$
5.	T9 (alluvial plain)–T7 (fluviomarine Plain)	Quartz Wustite Diaspore Calcite Ferrhydrite Albite Kaolinite Halloysite	$3.899 \times 10^{-3} \text{Albite}_{(s)} + 1.5596 \times 10^{-2} \text{H}^+_{(aq)} + 5.8485 \times 10^{-3} \text{H}_2\text{O}_{(l)} + 1.9495 \times 10^{-3} \text{Diaspore}_{(s)} + 1.9495 \times 10^{-3} \text{Ferrhydrite}_{(s)} + 1.9495 \times 10^{-3} \text{Anorthite}_{(s)} + 1.9495 \times 10^{-3} \text{H}_2\text{CO}_{3(s)} \rightarrow 5.8485 \times 10^{-3} \text{Quartz}_{(s)} + 3.899 \times 10^{-3} \text{Na}^+_{(aq)} + 3.899 \times 10^{-3} \text{Gibbsite}_{(s)} + 5.8485 \times 10^{-3} \text{H}_4\text{SiO}_{4(s)} + 1.9495 \times 10^{-3} \text{Al}^{3+}_{(aq)} + 1.9495 \times 10^{-3} \text{Fe}^{3+}_{(aq)} + 1.9495 \times 10^{-3} \text{Ca}(\text{HCO}_3)_2_{(s)} + 1.9495 \times 10^{-3} \text{Kaolinite/Halloysite}_{(s)}$
6.	T8 (fluviomarine plain)–T7 (fluviomarine plain)	Quartz Albite Diaspore Anorthite Ferrhydrite Halloysite Kaolinite	$3.672 \times 10^{-2} \text{H}_2\text{O}_{(l)} + 1.224 \times 10^{-2} \text{Diaspore}_{(s)} + 2.448 \times 10^{-2} \text{H}^+_{(aq)} + 2.448 \times 10^{-2} \text{Albite}_{(s)} + 1.224 \times 10^{-2} \text{Fe}^{3+}_{(aq)} \rightarrow 1.224 \times 10^{-2} \text{H}_4\text{SiO}_{4(s)} + 1.224 \times 10^{-2} \text{Al}^{3+}_{(aq)} + 1.224 \times 10^{-2} \text{Kaolinite/Halloysite}_{(s)} + 3.672 \times 10^{-2} \text{Quartz}_{(s)} + 2.448 \times 10^{-2} \text{Na}^+_{(aq)} + 1.224 \times 10^{-2} \text{Ferrhydrite}_{(s)}$
		Quartz Albite	

Table 5 (continued)

Nos.	Flows	Minerals	Mineral reactions
7.	T4 (old-beach ridge)-T1 (fluviomarine plain)	Diaspore Ferrohydrite Halloysite	Anorthite Albite $1.2834 \times 10^{-4} \text{ Albite}_{(s)} + 3.2085 \times 10^{-4} \text{ H}^+ + 6.417 \times 10^{-5} \text{ H}_2\text{O}_{(l)} + 6.417 \times 10^{-5} \text{ Ferrohydrite}_{(s)} + 6.417 \times 10^{-5} \text{ Anorthite}_{(s)} + 6.417 \times 10^{-5} \text{ H}_2\text{CO}_{3(s)} \rightarrow 1.2834 \times 10^{-4} \text{ Kaolinite}_{(s)} / \text{Halloysite}_{(s)} + 1.9251 \times 10^{-4} \text{ Quartz}_{(s)} + 1.2834 \times 10^{-4} \text{ Na}^+_{(aq)} + 6.417 \times 10^{-5} \text{ H}_4\text{SiO}_{4(s)} + 6.417 \times 10^{-5} \text{ Fe}^{3+}_{(aq)} + 6.417 \times 10^{-5} \text{ Ca}(\text{HCO}_3)_2(s)$
8.	T4 (old-beach ridge)-T3 (swale)	Quartz Ferrohydrite Kaolinite Ferrohydrite	Anorthite Cristobalite Pyrite $1.074 \times 10^{-3} \text{ Pyrite} + 3.759 \times 10^{-3} \text{ O}_2 + 1.611 \times 10^{-3} \text{ H}_2\text{O} \rightleftharpoons 1.074 \times 10^{-3} \text{ Wustite} + 1.074 \times 10^{-3} \text{ H}_2 + 1.074 \times 10^{-3} \text{ H}^+ + 2.148 \times 10^{-3} \text{ SO}_4^{2-}$
9.	T3 (swale)-T2 (young-beach ridge and sand dune complex)	Wustite Quartz	Cristobalite $7.99 \times 10^{-6} \text{ Ferrohydrite}_{(s)} + 3.995 \times 10^{-5} \text{ H}^+ + 1.598 \times 10^{-5} \text{ Albite}_{(s)} \rightarrow 7.99 \times 10^{-6} \text{ H}_4\text{SiO}_{4(s)} + 7.99 \times 10^{-6} \text{ Fe}^{3+}_{(aq)} + 7.99 \times 10^{-6} \text{ Kaolinite}_{(s)} / \text{Halloysite}_{(s)} + 2.397 \times 10^{-5} \text{ Quartz}_{(s)} + 1.598 \times 10^{-5} \text{ Na}^+_{(aq)}$
		Ferrohydrite	Albite

such as albite, cristobalite, orthoclase, and quartz. Oxide minerals and ferrihydrite, in particular, are also found in this unit. The saturation indices in the young-beach ridge and sand dune complex show that the silicate mineral was supersaturated (precipitated). This is because the concentration of SiO_2 in this area is relatively high. The concentration of $\text{Fe}_{(\text{total})}$ at T2 increased from the previous point, T3 (swale), because of the ferrihydrite dissolution.

4.4 Inverse Modeling for Hydrogeochemical Process

Table 5 shows the mass balance reaction based on inverse modeling results for each flow path in the study area. Further, Fig. 9 denotes the facies and hydrogeochemical processes in each of the landforms in the form of a map. The results of inverse modeling at flow path 1 (denudational hills of the Old-andesite formation T11—alluvial plain T10) show that minerals such as albite, diaspore, ferrihydrite, and anorthite were undersaturated (dissolution). Consequently, some of the hydrochemical constituents— Ca^{2+} , Na^+ , HCO_3^- , $\text{Fe}_{(\text{total})}$, and SiO_2 —were increasing in the alluvial plain (T10). The dissolution of albite explains the escalation of SiO_2 and Na^+ , while the dissolution of albite would increase the concentration of Na^+ , and the dissolution of ferrihydrite would do the same for $\text{Fe}_{(\text{total})}$. Based on the model, it would take 6.45×10^{-3} mmol of albite to produce 6.45×10^{-3} mmol of Na^+ , while increasing the concentration of $\text{Fe}_{(\text{total})}$ by 3.225×10^{-3} mmol would be caused by the dissolution of 3.225×10^{-3} mmol of ferrihydrite.

Additionally, there is a unique finding at this path where a derivative process occurs, namely dissolution of calcium–bicarbonate as a result of the breakdown of anorthite. The calcium–bicarbonate then produces calcite, carbon dioxide, and water. Subsequently, calcite could break down into Ca^{2+} and HCO_3^- that increasing the alkalinity and Ca^{2+} in this path. The interesting thing is that the calcite found in T10 does not originate from the sedimentation process as in the denudational hills of the Sentolo formation (T12) and the eastern alluvial plain (T9); in fact, it is a derivative process from anorthite.

The chemical constituents of the alluvial plain (T10) show that Al^{3+} had decreased from the previous measurement point (T11). Nevertheless, the inverse model shows there was a release of as much as 3.225×10^{-3} mmol of Al^{3+} as a product of the dissolution of diaspore. There are several possibilities that could explain the decline in Al^{3+} concentration. The first is that Al^{3+} can be deposited with water molecules to form gibbsite. The second possibility is that Al^{3+} was precipitated together with ortho-silicic acid and water to form kaolinite. Ortho-silicic acid can be found in T10 as a result of the dissolution of quartz, although the concentration of dissolved quartz is smaller than precipitated quartz due to the dissolution of some minerals such as albite. Furthermore, quartz in T10 can react with hydrogen gas to produce SiO_2 and water, a reaction that would also explain the increasing concentration of SiO_2 in T10.

The chemical constituents of the alluvial plain (T10) show that Al^{3+} had decreased from the previous measurement point (T11). Nevertheless, the inverse model shows there was a release of as much as 3.225×10^{-3} mmol of Al^{3+} as a product of the dissolution of diaspore. There are several possibilities that could explain the decline in Al^{3+} concentration. The first is that Al^{3+} can be deposited with water molecules to form gibbsite. The second possibility is that Al^{3+} was precipitated together with ortho-silicic acid and water to form kaolinite. Ortho-silicic acid can be found in T10 as a result of the dissolution of quartz, although the concentration of dissolved quartz is smaller than precipitated quartz due to the dissolution of some minerals such as albite. Furthermore,

quartz in T10 can react with hydrogen gas to produce SiO_2 and water, a reaction that would also explain the increasing concentration of SiO_2 in T10.

The inverse model in the flow path from T10 (alluvial plain) to T6 (fluviomarine plain) shows that albite, anorthite, and pyrite were dissolving, while quartz, kaolinite/halloysite, and ferrihydrite were being precipitated. Here there was an increasing amount of Ca^{2+} , Na^+ , HCO_3^- , and Al^{3+} concentration and a decreasing amount of SiO_2 triggered by the release and exchange of ions between groundwater and minerals. The SO_4^{2-} rose due to pyrite reduction, with the inverse modeling results concurring that the pyrite was dissolving to produce 8.27×10^{-4} mmol ferrihydrite, 1.654×10^{-3} mmol SO_4^{2-} , and 1.654×10^{-3} mmol hydrogen. Iron underwent oxidation, from + 2 ions in the pyrite to + 3 ions in ferrihydrite, while sulfur was reduced, from - 1 in the pyrite to - 3 in the SO_4^{2-} . Therefore, at T6 there was a pyrite reduction process causing dissolved SO_4^{2-} levels in the groundwater to rise. Further, the increasing concentration of $\text{Fe}_{(\text{total})}$ could also occur due to the released $\text{Fe}_{(\text{total})}$ into the groundwater owing to the weathering or dissolution of ferrihydrite.

The path from T5 (old-beach ridge) toward T6 (fluviomarine plain) generates inverse modeling showing that the minerals on the dissolution phase were anorthite and ferrihydrite, while albite and kaolinite have been on the precipitated condition. The chemical constituents in T6, which has decreased from T5, were Mg^{2+} , K^+ , and SiO_2 . Precipitation of 5.586×10^{-4} mmol albite in this system requires 1.1172×10^{-3} mmol SiO_2 and 5.586×10^{-4} mmol Na^+ . The reduction of SiO_2 in this system can be caused by this reaction. This system also produces a lot of kaolinite/halloysite, such as the results of precipitation of kaolinite/halloysite due to the dissolution of gibbsite and as a result of dissolving of anorthite.

The results of the inverse modeling for the flow path from T12 (denudational hill of the Sentolo formation) to T9 (alluvial plain) show varied results. Dissolution occurred in diaspore, ferrihydrite, albite, anorthite, wustite, and calcite. The minerals produced in this system were gibbsite, quartz, and kaolinite/halloysite. Chemical constituents which have increased were Ca^{2+} , Na^+ , K^+ , HCO_3^- , Al^{3+} , and $\text{Fe}_{(\text{total})}$, while Mn^{2+} and SiO_2 have decreased. The increase in Ca^{2+} and HCO_3^- in this system (T9) possibly occurred due to the dissolution of calcite. Based on the mass balance calculation, the dissolution of 1.591×10^{-3} mmol of calcite would be relinquished as much as 1.591×10^{-3} mmol of Ca^{2+} and HCO_3^- . The 3.182×10^{-3} mmol albite mineral at T9 dissolved to produce 1.591×10^{-3} mmol kaolinite/halloysite, 6.364×10^{-3} mmol quartz, and the release of 3.182×10^{-3} mmol Na^+ . The dissolution of albite was one of the causes of the increasing concentration of Na^+ in this unit. The increase in Al^{3+} occurred because of the dissolution of the diaspore, where Al^{3+} was released at a level of 1.591×10^{-3} mmol. The increase in $\text{Fe}_{(\text{total})}$ also occurred due to the dissolution of 1.591×10^{-3} mmol ferrihydrite.

The inverse modeling in the flow path from T9 (alluvial plain) to T7 (fluviomarine plain) reveals a varied mineral response in which halloysite, ferrihydrite, and albite undergo a dissolution process, while precipitation occurs in quartz, diaspore, and anorthite. The chemical constituents that increased in this system were Na^+ , K^+ , HCO_3^- , $\text{Fe}_{(\text{total})}$, and quartz, while Ca^{2+} and Al^{3+} declined. In this model, kaolinite/halloysite initially dissolved because of it is undersaturated, producing 3.899×10^{-3} mmol gibbsite. However, due to the dissolution of albite (which also produces kaolinite/halloysite products), this mineral ended up being precipitated. The dissolution of albite was also responsible for the 3.899×10^{-3} mmol increase in Na^+ . The increase in Fe^{3+} and Al^{3+} was still ongoing at this point due to the dissolution of ferrihydrite and diaspore, both of which dissolved by as much as 1.9495×10^{-3} mmol (which also occurs in T9).

The inverse modeling from T8 (fluviomarine plain) to T7 (fluviomarine plain, the confluence point) suggests that the minerals diaspore and albite were dissolving, while kaolinite/halloysite, quartz, and ferrihydrite were precipitating. This saw an increase in Al^{3+} , SiO_2 , Na^+ , and $\text{Fe}_{(\text{total})}$. The increase of Al^{3+} occurred due to the dissolution of diaspore, releasing 1.224×10^{-2} mmol Al^{3+} to the groundwater. Quartz had been on the dissolution phase at this point, but the dissolution of albite led to increased precipitation of quartz. The dissolution of albite minerals was also responsible for increasing Na^+ by 2.448×10^{-2} mmol. In this flow path, the model showed precipitation of ferrihydrite and a resulting fall in $\text{Fe}_{(\text{total})}$ concentration. However, since T7 was the confluence point, where there was some recharge from the other groundwater systems (T9), which caused the dissolution of ferrihydrite minerals and an overall rise in $\text{Fe}_{(\text{total})}$ concentration.

Further examination reveals that the mixing process is likely to occur in the fluviomarine plain, especially in the eastern part. The first reason is that the fluviomarine plain is supplied by two groundwater from different geomorphological units (and, of course, from two types of groundwater). This unit becomes the assembly point of groundwater movements, as evidenced by electrical conductivity that relatively high (up to 2300 $\mu\text{S}/\text{cm}$). Referring to Mazor et al. (1993), which explains that the mixing process between two types of water can induce minerals, the minerals in this unit have a different response in terms of its saturation condition. The impact, which is also becoming the second reason, is that the water–rock interaction process in this unit has a different magnitude between groundwater coming from the alluvial plain and old-beach ridge. Therefore, the combination of information from the flow net data and inverse modeling shows the possibility of mixing in the fluviomarine plain.

The inverse modeling provides evidence that the dissolution of ferrihydrite, albite, and anorthite minerals and the precipitation of halloysite and quartz occurred in the flow path from T4 (old-beach ridge) to T1 (fluviomarine plain). Meanwhile, kaolinite and cristobalite were in the equilibrium phase. Hydrochemical data of groundwater at T1, if compared to T3, saw an increase in Ca^{2+} , Mg^{2+} , HCO_3^- , Al^{3+} , and $\text{Fe}_{(\text{total})}$, while SiO_2 ions have decreased. The results of the inverse modeling in the T3 (Swale) toward T2 (young-beach ridge and sand dune complex) revealed that ferrihydrite and albite minerals were undersaturated, while quartz was supersaturated. The chemical constituents which fluctuated due to the mass transfer process from minerals were SiO_2 , $\text{Fe}_{(\text{total})}$, Na^+ , and Al^{3+} .

Inverse modeling of the groundwater system from T4 (old-beach ridge) to T3 (swale) generates that ferrihydrite and pyrite were dissolving, while wustite had been saturated. The ions that fluctuated due to the process of water–rock interaction at T3 were SO_4^{2-} s and $\text{Fe}_{(\text{total})}$. This is because the minerals in the swale landform were mostly composed of $\text{Fe}_{(\text{total})}$ and SO_4^{2-} . Although ferrihydrite dissolution occurred in this unit, the decrease in $\text{Fe}_{(\text{total})}$ content was caused by the massive deposition of wustite, which required more iron resulting in a deficit of iron in groundwater. The increase in SO_4^{2-} levels in the swale was relatively significant due to the predominance of the pyrite in this unit. In terms of the uplifting of Ca^{2+} , Machusak and Kump (1997) explain that the concentration of alkalinity and Ca^{2+} in groundwater is also likely to be caused by a combination of aerobic metabolism, carbonate dissolution, and SO_4^{2-} reduction. The model is not suitable to explain the rise of Ca^{2+} in swale because reduction did not occur and no carbonate minerals found in this unit (its existence is still limited to the hypothesis).

There is a unique finding in this unit that the secondary minerals will be formed due to the dissolution of the mineral pyrite, namely gypsum, as explained by Logan and Nicholson (1997) in their conceptual model. Gypsum chain reaction can trigger an upsurge in SO_4^{2-} and Ca^{2+} content (Abdel Wahed et al. 2015). Furthermore, Ca^{2+} binds HCO_3^- to

calcite, which can cause a decrease in HCO_3^- content. Recalling the hydrogeochemical data in the swale unit (Table 2), the formation of gypsum and calcite should occur due to an increase in Ca^{2+} and SO_4^{2-} levels that are quite massive and a decrease in HCO_3^- levels. If this happens, then one of Machusak and Kump's (1997) arguments related to the increase in Ca^{2+} due to calcite dissolution is suitable for this unit. However, XRD results from the drilling of minerals as deep as two meters did not reveal any of these minerals. There are two possibilities that can occur in this unit. First, the formation of calcite and gypsum is located in a deeper layer (more than two meters below the surface). Another possibility is that the formation has not or did not occur, where the dissolution of pyrite directly releases iron into the groundwater system, as is presented in inverse modeling result (Table 5). The formation of gypsum seems to be a very rational explanation. According to Li (1995), the dissolution of gypsum is responsible for simultaneously increasing Ca^{2+} and SO_4^{2-} levels.

5 Conclusions

The research area in the southern part of Kulonprogo consists of several geomorphological units, namely denudational hills, alluvial plain, fluvio-marine plain, old-beach ridge, swale, young-beach ridge and sand dune complex, and beach. In general, the variety of hydrogeochemical processes that occur in each geomorphological unit is responsible for the typical hydrogeochemical characteristics. The particular landform layout has an impact on the direction of groundwater flow in the study area due to the morphological characteristics of each unit. In terms of vertical extent, the altitude of denudational hills is comparatively higher than subsequent units, namely alluvial plains, etc. Therefore, the direction of groundwater movement in the research area flows from north to south regionally. However, if it were reviewed locally, the groundwater movement would be seen to start from the denudational hills and flow toward the fluvio-marine plain in a north to south direction. The beach ridge, on the other hand, has a slightly higher elevation than the surrounding units (swale and fluvio-marine plain) so that the direction of flow is toward the north, from the old-beach ridge to the fluvio-marine plain.

Each geomorphology unit also influences the residence time of groundwater, because one of the most important aspects of geomorphology is the slope. This is indicated by the concentration of TDS, which tends to be highest at the groundwater's endpoint, such as at the fluvio-marine plain (T5, T6, T7, T8, T9). These areas have a flat slope rate compared to the recharge area (denudational hills—T11 & T12). This phenomenon does not happen in beach ridge, swale, sand dune complex, and beach, however, which are included as a local aquifer recharging directly via rainwater, leading to a TDS value that is quite low.

The variety of landform units also controls the existence of minerals and their distribution. This is due to passive morphogenesis, where each landform is closely related to its constituent lithology and geological formation. In this study area, there are three major geological formations: (1) Old-andesite formation that provides volcanic genesis information in the past where the constituent material is mainly old volcanic rocks such as andesite; (2) Sentolo formation which indicates marine depositional conditions in the past leading to limestones as a result of marine organism transformation; and (3) alluvium formation which is a landform composed of alluvium material from upstream.

The consequence of the varied geomorphological aspects (landforms) is that the groundwater in each landform has a typical hydrochemical constituent's characteristic of the hydrogeochemical processes happening there. The hydrogeochemical processes

that occur in denudational hills toward alluvial plains are the dissolution of hydroxide-oxide (wustite and ferrihydrite), albite, diaspore, calcite, and gibbsite. Consequently, there is a tendency toward increasing concentrations of Na^+ , quartz, $\text{Fe}_{(\text{total})}$, Ca^{2+} , and Al^{3+} . The process of ion exchange on albite and diaspore and the reduction process in the form of half-reaction in ferrihydrite (if Fe^{2+} is formed) also occurs in this unit. The dissolution of albite is still continuing in the flow path from alluvial plains to fluvio-marine plain, and this causes an increase in Na^+ and SiO_2 , leading to quartz minerals being precipitated. Oxide-hydroxide minerals such as ferrihydrite are also being dissolved, leading to an increase in $\text{Fe}_{(\text{total})}$ concentration.

Groundwater from the old-beach ridge to the fluvio-marine plain witnesses the dissolution of ferrihydrite, which causes an increase of $\text{Fe}_{(\text{total})}$; albite also dissolves, causing an increase in Na^+ and SiO_2 and the precipitation of quartz. Similarly, in the fluvio-marine plain, groundwater from the old-beach ridge to the swale, young-beach ridge, and sand dune complex, also experienced a dissolution of oxide-hydroxide minerals, in particular, ferrihydrite and pyrite, that increases the concentration of Fe^{3+} . Fe^{2+} levels, on the other hand, decrease because wustite tends to precipitate out. Na^+ and SiO_2 also increase due to the dissolution of albite. Also, the mixing process between two different hydrogeochemical facies, which occurs in the fluvio-marine plain, is responsible for changing the chemical constituents in water.

Acknowledgements This research was part of a bachelor's degree thesis in the Faculty of Geography, Universitas Gadjah Mada, Indonesia. The authors would like to thank Aldza Rausan Dzakwani, Melati Ayuning Putri, Aprilia Nur Widyastuti, Syiva Fauzia, Yanti Kusmiati, and Tania Dewanti for their assistance in the collection of field data. This research did not receive any specific grant from funding agencies in the public, commercial, or not-for-profit sectors.

References

- Abdel Wahed MSM, Mohamed EA, El-Sayed MI, M'nif A, Sillanpää M (2015) Hydrogeochemical processes controlling the water chemistry of a closed saline lake located in Sahara Desert: Lake Qarun, Egypt. *Aquat Geochem* 21(1):31–57. <https://doi.org/10.1007/s10498-015-9253-3>
- Adji TN, Sejati SP (2014) Identification of groundwater potential zones within an area with various geomorphological units by using several field parameters and a GIS approach in Kulonprogo Regency, Java, Indonesia. *Arabian J Geosci* 7:161. <https://doi.org/10.1007/s12517-012-0779-z>
- Adji TN, Widyastuti M (2005) Application of inverse modeling technique to describe hydrogeochemical processes responsible to spatial distribution of groundwater quality along flowpath. *Indones J Geogr* 37(2):85–102
- Alpers CN, Nordstrom DK (1999) Geochemical modeling of water–rock interactions in mining environments, chapter 14. In: Plumlee GS, Logsdon MJ (eds) *The environmental geochemistry of mineral deposits. Part A. Processes, methods, and health issues*. Society of Economic Geologists, Littleton, Colorado, *Reviews in Economic Geology*, vol 6A, pp 289–323
- Appelo CAJ, Postma D (2005) *Geochemistry, groundwater, and pollution*, 2nd edn. A.A. Balkema Publishers, Amsterdam
- Belkhir L, Mouni L, Tiri A (2011) Water–rock interaction and geochemistry of groundwater from the Ain Azel aquifer, Algeria. *Environ Geochem Health* 34(1):1–13. <https://doi.org/10.1007/s10653-011-9376-4>
- Blanchette D, Lefebvre R, Nastev M, Cloutier V (2010) Groundwater quality, geochemical processes and groundwater evolution in the Chateauguay River Watershed, Quebec, Canada. *Can Water Resour J* 35(4):503–526. <https://doi.org/10.4296/cwrj3504503>
- Chilingar GV (1956) Durov's classification of natural waters and chemical composition of atmospheric precipitation in the USSR: a review. *Am Geophys Union* 37:193–196

- Cloutier V, Lefebvre R, Savard MM, Bourque E, Therrien R (2006) Hydrogeochemistry and groundwater origin of the Basses-Laurentides sedimentary rock aquifer system, St. Lawrence Lowlands, Quebec, Canada. *Hydrogeol J* 14:573–590
- Dana ES (1949) *Mineralogy*. Wiley, New York
- Darcy H (1856) *Les Fontaines Publiques de la Ville de Dijon*. Dalmont, Paris
- de Marsily G (1986) *Quantitative hydrogeology*. Academic Press, Orlando
- Domenico PA, Schwartz FW (1998) *Physical and chemical hydrogeology*. Wiley, New York
- Dragon K, Gorski J (2012) Identification of groundwater chemistry origins in a regional aquifer system (Wielkopolska region, Poland). *Environ Earth Sci* 72(5):2153–2167. <https://doi.org/10.1007/s12665-014-3567-0>
- Edmunds WM, Shand P (2008) Groundwater baseline quality. In: Edmunds WM, Shand P (eds) *Natural groundwater quality*. Blackwell Publishing, Malden, pp 1–21
- El-Kadi AI, Plummer L, Aggarwal P (2011) NETPATH-WIN: an interactive user version of the mass-balance model, NETPATH. *Groundwater* 49:593–599. <https://doi.org/10.1111/j.1745-6584.2010.00779.x>
- Frape SK, Fritz P, McNutt RH (1984) Water–rock interaction and chemistry of groundwaters from the Canadian Shield. *Geochim Cosmochim Acta* 48(8):1617–1627
- Furi W, Razaek M, Abiye TA, Kebede S, Legesse D (2012) Hydrochemical characterization of complex volcanic aquifers in a continental rifted zone: the middle Awash basin, Ethiopia. *Hydrogeol J* 20(2):385–400. <https://doi.org/10.1007/s10040-011-0807-1>
- Gray WG, Miller CT (2004) Examination of Darcy’s law for flow in porous media with variable porosity. *Environ Sci Technol* 38:22. <https://doi.org/10.1021/es049728w>
- Hadmoko DS, Lavigne F, Sartohadi J, Hadi MP, Winaryo (2010) Landslide hazard and risk assessment and their application in risk management and landuse planning in eastern flank of Menoreh mountains, Yogyakarta Province, Indonesia. *Nat Hazards* 54:623–642. <https://doi.org/10.1007/s11069-009-9490-0>
- Harsono P (1968) On the age of the Sentolo Formation based on planktonic foraminifera. Bandung Institute Technology, Department of Geology Control, No. 64, pp 5–21
- Helena B, Pardo R, Vega M, Barrado E, Fernandez JM, Fernandez L (2000) Temporal evolution of groundwater composition in an alluvial aquifer (Pisuerga River, Spain) by Principal Component Analysis. *Water Res* 34(3):807–816
- Hiscock KM, Bense VF (2014) *Hydrogeology: principles and practices*, 2nd edn. Wiley Blackwell, London
- Huggett RJ (2011) *Fundamentals of geomorphology*, 3rd edn. Routledge, New York
- Kadar D (1975) Planktonic foraminifera from the lower part of the Sentolo Formation, Central Java, Indonesia. *J Foraminifer Res* 5(1):1–20
- Khatri N, Tyagi S (2015) Influences of natural and anthropogenic factors on surface and groundwater quality in rural and urban areas. *Front Life Sci* 8(1):23–39. <https://doi.org/10.1080/21553769.2014.933716>
- King CAM (1972) *Beaches and coasts*. Edward Arnold, London
- Kresic N (2006) *Hydrogeology and groundwater modeling*, vol 2, 2nd edn. CRC Press, Boca Raton
- Li Y (1995) Geochemical mass balances of major chemical constituents in the watershed of the Changhuan River in China. *Aquat Geochem* 1(2):147–156. <https://doi.org/10.1007/bf00702888>
- Lloyd JW, Heathcote JA (1985) *Natural inorganic hydrochemistry in relation to groundwater*. Clarendon Press, Oxford
- Logan WS, Nicholson RV (1997) Origin of dissolved groundwater sulphate in coastal plain sediments of the Río de la Plata, Eastern Argentina. *Aquat Geochem* 3(4):305–328. <https://doi.org/10.1023/a:1009680326095>
- Luo W, Gao X, Zhang X (2018) Geochemical processes controlling the groundwater chemistry and fluoride contamination in the Yuncheng Basin, China—an area with complex hydrogeochemical conditions. *PLoS ONE* 13(7):e0199082. <https://doi.org/10.1371/journal.pone.0199082>
- MacDonald and Partner, Binnie and Partner Hunting Technical Service Ltd. (1984) Greater Yogyakarta groundwater resources study, Vol. 3 Groundwater, Indonesia. Groundwater Development Project (P2AT), Ministry of Public Works, Government of Republic Indonesia
- Machusak DD, Kump LR (1997) Environmental controls on groundwater chemistry in an offshore island aquifer: Fiesta Key, Florida. *Aquat Geochem* 3(2):129–167. <https://doi.org/10.1023/a:1009648200301>
- Mazor E, Drever JI, Finley J, Huntoon PW, Lundy DA (1993) Hydrochemical implications of groundwater mixing: an example from the Southern Laramie Basin, Wyoming. *Water Resour Res* 29(1):193–205. <https://doi.org/10.1029/92wr01680>
- Nielsen DM, Nielsen GL (2006) *The essential handbook of groundwater sampling*. CRC Press, Boca Raton
- Nordstrom DK, Ball JW, Donahoe RJ, Whitemore D (1989) Groundwater chemistry and water–rock interactions at Stripa. *Geochim Cosmochim Acta* 53(8):1727–1740
- Nourtier-Mazaauric E, Guy B, Fritz B, Borsse E, Garcia D, Clément A (2005) Modelling the dissolution/precipitation of ideal solid solutions. *Oil Gas Sci Technol* 60(2):401–415

- Pacheco F, van der Weijden CH (1996) Contributions of water–rock interactions to the composition of groundwater in areas with a sizeable anthropogenic input: a case study of the waters of the Fundão Area, Central Portugal. *Water Resour Res* 32(12):3553–3570
- Parkhurst DL, Appelo CAJ (1999) User's guide to PHREEQC (Version 2)—a computer program for speciation, batch-reaction, one-dimensional transport, and inverse geochemical calculations. U.S. Geological Survey, Water-Resources Investigations Report 99-4259, Washington
- Plummer LN, Parkhurst DL, Thorstenson DC (1983) The development of reaction models for ground-water systems. *Geochim Cosmochim Acta* 47:665–686
- Plummer LN, Prestemon EC, Parkhurst DL (1991) An interactive code (NETPATH) for modeling net geochemical reactions along a flow path. U.S. Geological Survey, Water-Resources Investigations Report 91-4078
- Rhoades JD, Kandiah A, Mashali A (1992) The use of saline waters for crop production. FAO, Rome
- Richardson JL, Wilding LP, Daniels RB (1992) Recharge and discharge of groundwater in aquatic conditions illustrated with flownet analysis. *Geoderma* 53:65–78
- Santosa LW (2012) Hidrostratigrafi Akuifer sebagai Geoindikator Genesis Bentuklahan di Wilayah Kepesiran Kabupaten Kulonprogo (Hydrostratigraphic aquifer as a geoindicator of landforms genesis in the coastal region of Kulonprogo Regency, Special Region of Yogyakarta). *Daerah Istimewa Yogyakarta. Forum Geogr* 26(2):160–177 (in Bahasa Indonesia with English abstract)
- Schot PP, van der Wal J (1992) Human impact on regional groundwater composition through intervention in natural flow patterns and changes in land use. *J Hydrol* 134:297–313
- Summerfield MA (2013) *Global geomorphology*, 2nd edn. Routledge, New York
- Sunarto (2014) *Geomorphology and contribution in the conservation of aeolian sand dune coast from agrogenic and urbanogenic disasters*. Inauguration Speech of Professor Position at the Faculty of Geography, Gadjah Mada University, Yogyakarta
- Syafri I, Budiadi E, Sudradjat A (2013) Geotecnic configuration of Kulon Progo Area, Yogyakarta. *Indones J Geol* 8(4):185–190
- Todd DK, Mays LW (2005) *Groundwater hydrology*, 3rd edn. Wiley, New York
- van Bemmelen RW (1949) *The geology of Indonesia: general geology of Indonesia and adjacent archipelagoes*. Government Printing Office, The Hague
- van Zuidam RA (1983) *Guide to geomorphology aerial photographic interpretation and mapping*. ITC Enschede, Enschede
- van Zuidam RA (1985) *Aerial photo—interpretation in terrain analysis and geomorphological mapping*. Smith Publisher, The Hague
- Verstappen TH (1983) *Applied geomorphology: geomorphology surveys fir environment development*. Elsevier, Amsterdam
- Widagdo I, Pramumijoyo S, Harijoko A (2018) Tectonostratigraphy-volcanic of Gajah-ljo-Menoreh Tertiary volcanic formations in Kulon Progo mountain area, Yogyakarta-Indonesia. *IOP Conf Ser Earth Environ Sci* 212:012052
- Winter TC, Harvey JW, Franke OL, Alley WM (1998) *Ground water and surface water a single resource*. U.S. Geological Survey Circular 1139. U.S. Government Printing Office, Denver
- Younger PL (2007) *Groundwater in the environment*. Blackwell Publishing, Oxford
- Zaporozec A (1972) Graphical interpretation of water-quality data. *Ground Water* 10(2):32–43
- Zinck JA, Metternicht G, Bocco G, Valle HFD (2016) *Geopedology: an integration of geomorphology and pedology for soil and landscape studies*. Springer, Cham

Publisher's Note Springer Nature remains neutral with regard to jurisdictional claims in published maps and institutional affiliations.